drones

Article

Assessing the Carbon Mitigation Potential of UAV-Based Last-Mile Delivery Using 3D Path Planning: A Case Study of Shanghai

Ruiqi Wang [1,2] and Yang Liu [1,*]

[1] Key Laboratory of Land Surface Pattern and Simulation, Institute of Geographic Sciences and Natural Resources Research, Chinese Academy of Sciences, Beijing 100101, China
[2] School of Information Science and Technology, Beijing Foreign Studies University, Beijing 100089, China; 202320102021@bfsu.edu.cn
* Correspondence: liu_yang@igsnrr.ac.cn

Highlights

What are the main findings?

- A unified UAV–courier carbon accounting framework was developed using 185,673 real parcel orders and 3D urban spatial data in Shanghai.
- Under the modeled assumptions, UAV delivery tends to show lower per-delivery carbon emissions under lightweight and high-speed operating conditions, with a scenario-based annual reduction estimate of about 343,300 t CO_2 by 2030.

What are the implications of the main findings?

- The climate benefits of low-altitude logistics are highly condition-dependent and should be guided by payload, speed, and deployment scenarios.
- The proposed framework provides quantitative support for urban low-altitude logistics planning, infrastructure layout, and carbon-reduction policy design in Chinese megacities.

Abstract

Urban last-mile delivery is an increasingly important source of transport-related emissions, yet evidence on low-altitude logistics under real-order demand and urban spatial constraints remains limited. Taking Shanghai as a representative megacity, this study integrates 185,673 real parcel orders with 3D urban spatial data to develop a unified unmanned aerial vehicle (UAV)–courier carbon accounting framework. The framework combines 3D UAV route-planning algorithms, UAV energy-consumption models, electric courier-vehicle energy models, and grid emission factors to compare carbon emissions between UAV and conventional delivery modes. The results show that, under the modeled operating assumptions, UAV delivery tends to provide lower per-delivery carbon emissions under lightweight and high-speed operating conditions. Scenario analysis further suggests that UAV deployment in Shanghai could reduce carbon emissions by approximately 343,300 t CO_2 annually by 2030. These findings provide quantitative support for urban low-altitude logistics planning, infrastructure deployment, and policy design for low-carbon last-mile delivery. The framework is transferable to other Chinese cities with similar urban conditions, but the numerical results require local recalibration of parcel demand, urban morphology, airspace constraints, and electricity-related carbon factors.

Academic Editor: Yu-Jun Zheng

Received: 24 March 2026
Revised: 22 April 2026
Accepted: 7 May 2026
Published: 11 May 2026

Keywords: unmanned aerial vehicles (UAVs); last-mile delivery; low-altitude logistics; carbon emissions; 3D path planning

1. Introduction

Since the mid-20th century, global greenhouse-gas emissions dominated by CO_2 have risen rapidly, and climate warming has become a critical environmental challenge constraining sustainable human development [1]. Energy consumption from the transport sector is among the most important emitting activities, accounting for 15% of carbon emissions [2]. With the rapid growth of e-commerce and on-demand delivery, urban-logistics emissions may rise by 60% by 2030 [3].

China is both one of the world's largest greenhouse-gas emitters and a pivotal actor in advancing global climate governance [4]. In 2020, the Chinese government set the "Carbon peaking and carbon neutrality" goals—achieving carbon peaking before 2030 and carbon neutrality before 2060—and subsequently strengthened its Nationally Determined Contributions (NDCs) [5]. However, structural challenges persist due to new coal-fired power additions and energy-intensive industries, underscoring an urgent need to identify new mitigation opportunities at the city level and within specific sectors [6–8].

Carbon-emission impacts of urban logistics—particularly parcel-express and food-delivery services—have drawn increasing attention. Taking food delivery as an example, Zhong et al. [9] quantitatively assessed the carbon emissions of food-delivery systems in 270 Chinese cities using the IPCC emission-factor approach and multi-source big data, showing that nationwide food-delivery transport and packaging emitted approximately 1.67 Mt CO_2-eq in 2019. Although the study focused on food delivery, the underlying characteristics of high-frequency, small-parcel, time-sensitive on-demand urban delivery are highly similar to express services such as intra-city parcels and same-day delivery, suggesting substantial mitigation potential in the last-mile delivery domain.

To curb carbon emissions and air pollution from conventional fuel-powered vehicles, many Chinese cities have widely adopted large electric three-wheelers and electric two-wheelers for last-mile delivery [10,11]. Replacing diesel trucks with electric three-wheelers for "last-mile" delivery can markedly reduce greenhouse-gas emissions and energy consumption and, under certain conditions, improve operational efficiency [10,11]. However, under an electricity mix still dominated by fossil fuels and intensifying urban road congestion, even electric three-wheeler systems have emissions that are largely determined by factors such as grid carbon intensity and route efficiency [12]. Therefore, it is necessary to explore more innovative urban logistics models. In recent years, low-altitude logistics represented by unmanned aerial vehicles (UAVs) has been regarded as a promising technological pathway for urban last-mile delivery. Based on life-cycle assessment, Stolaroff et al. [13] showed that, for small-parcel delivery, small electric multirotor UAVs may outperform conventional trucks in energy use and greenhouse-gas emissions per parcel-kilometer.

In China, the "low-altitude economy" has been incorporated into national and local strategies, and emerging low-altitude logistics is viewed as a key avenue for fostering new-quality productive forces and advancing smart cities [14]. Recent studies suggest that low-altitude logistics offers distinctive advantages in improving delivery efficiency, alleviating pressure on ground traffic, and enhancing emergency-supply dispatch capacity [15–19]. Media analyses suggest that China is expanding UAV logistics pilot programs; over the next five years, UAVs are expected to handle more than 5% of nationwide commercial delivery volume, and the market size associated with the low-altitude economy is projected to reach Renminbi (RMB) 3.5 trillion [20]. In highly urbanized regions such as the Yangtze River

Delta, UAV delivery networks built on facilities such as rooftop takeoff and landing sites and community micro-warehouses have entered the demonstration phase [21], providing a practical basis for exploring low-carbon transitions in urban last-mile logistics.

Although environmental impact assessments of UAV delivery are increasing internationally, most existing studies benchmark "UAVs vs. fuel trucks," and pay insufficient attention to the scenario of "UAVs replacing existing electric three-wheeler systems" [22–25]. In cities such as Shanghai—characterized by high population density, complex built forms, and widespread adoption of electric two- and three-wheelers—future grid decarbonization and the build-out of low-altitude logistics infrastructure will profoundly reshape the carbon-emission profiles of different delivery modes [26]. Therefore, it is necessary to develop 2030-oriented scenario assumptions and quantitatively compare CO_2 emissions under two modes: maintaining electric three-wheeler delivery versus partially or fully shifting to UAV delivery.

Building on the Shanghai subset of the Last-mile Delivery (LaDe) dataset [27], we further incorporate spatial data such as building heights, no-fly zones, and station points of interest (POIs) to construct a UAV–courier comparison framework for assessing energy-use and carbon-emission differences across last-mile delivery modes. On the basis of the 3D grid path-planning framework proposed by Sartori et al. [28], we adopt their 3D-grid Theta* implementation and define a flyable 3D space using Shanghai's building-height and no-fly-zone constraints to generate routes for large-scale orders. This study makes the following contributions:

1. Using more than 185,000 real last-mile orders, we examine carbon-emission differences between UAV delivery and conventional delivery under actual last-mile order settings.
2. We innovatively incorporate 3D urban spatial constraints from a representative megacity to develop an energy–carbon assessment framework for UAV last-mile delivery that more closely reflects constrained urban flight conditions than purely scenario-based assumptions.
3. We synthesize evidence and methods across multiple research dimensions relevant to low-altitude last-mile logistics to compare the carbon emissions of conventional delivery and UAV-based delivery. These studies have not yet been systematically integrated within a single low-altitude logistics scenario, yet they provide critical data and methodological foundations for assessing emissions from low-altitude logistics.

2. Related Work

Existing research on UAV-related carbon emissions has been conducted from multiple perspectives. This section reviews relevant studies from both domestic and international literature across six dimensions.

2.1. State of Research on Last-Mile Delivery

Last-mile delivery, also known as "last-mile" delivery, refers to the final segment of the logistics chain from sorting centers to end consumers, and it accounts for 30–50% of total logistics costs. Many studies set in the context of urban last-mile delivery focus on delivery route optimization [29–31], arrival-time prediction [32–34], and facility or depot location and distribution [35].

However, the last-mile delivery field has long lacked large-scale, publicly usable datasets. In 2023, the release of the LaDe dataset [27] filled this gap. It is the first public last-mile delivery dataset to cover on the order of tens of millions of parcels. Prior work on LaDe has benchmarked diverse deep learning models for tasks such as route prediction, estimated time of arrival (ETA) prediction, and spatiotemporal graph forecasting [27] but rarely examined the environmental impacts of last-mile delivery modes from a carbon-emissions perspective.

2.2. State of Research on UAV Energy Consumption

Unmanned delivery has recently attracted broad attention in urban last-mile applications, with delivery platforms primarily including autonomous ground vehicles and UAVs. Some studies focus on operational organization and scheduling [36], whereas others examine flight energy consumption [37].

Early measurement-based studies of UAV power-consumption models typically focused on a specific UAV and, based on experimental results, developed power models parameterized by flight speed and operating conditions [38]. Some power-consumption models were derived from analyses of battery performance [39].

Recent research developed a 2D closed-form model for multirotor UAV power consumption during horizontal and vertical flight and a 3D closed-form model for predicting multirotor UAV power consumption in general scenarios [40]; they further validated the models through extensive flight-data collection experiments, thereby providing a general model for estimating the energy use of UAV-based logistics delivery in low-altitude economy applications.

2.3. State of Research on Energy Use of Electric Transport Modes

The adoption of electric transport modes reduces carbon dioxide emissions and urban noise. Accordingly, their energy use and associated carbon emissions have received considerable attention [41]. Based on large-scale real-world on-road measurements, a recent study compiled energy-consumption data under real driving conditions for electric modes ranging from small e-scooters to large electric cars, providing a unified baseline for estimating average energy consumption of electric transport modes [42].

Many studies also focus on how speed influences energy consumption. Using extensive data linking battery energy use to electric-vehicle speed [43], some studies derived a speed–energy-consumption trend curve. Other studies directly used measurements collected during electric-vehicle driving to plot the relationship between vehicle speed and average energy consumption per unit distance [44].

Although electric road vehicles differ in mass, geometry, and duty cycle, they share several core powertrain characteristics that are relevant to energy-consumption modeling. In particular, electric drivetrains generally exhibit high tank-to-wheel efficiency, regenerative braking, and no idling losses; consequently, their energy use is governed mainly by vehicle mass, rolling resistance, aerodynamic drag, speed, and instantaneous power demand rather than by rated motor power alone [42]. A cross-vehicle synthesis further shows that mass-related energy-efficiency trade-offs are broadly consistent across electric vehicle classes, including larger electric two- and three-wheelers and passenger cars [42]. At the same time, real-world evidence from electric motorcycles indicates that electricity consumption is significantly affected by average running speed and deceleration-related driving behavior, supporting the relevance of speed-dependent proxy modeling for light electric courier vehicles [45].

2.4. State of Research on UAV Path Planning

Path planning is another foundational research direction for last-mile delivery and UAV logistics, and the methodological system for UAV path planning has become increasingly mature [46].

A variety of grid-based search algorithms have been developed, most of which are derived from A* [47], with extensions including LPA* [48], Focused D* [49], Theta* [50], and Lazy Theta* [51]. Among them, Theta* and Lazy Theta* outperform other methods, but they can be computationally slow on large-scale maps.

Recent studies used a family of 3D path-planning algorithms based on Theta* and Lazy Theta* to search for an initial polyline path from origin to destination [28] and proposed an approximately optimal 3D route-planning algorithm, which also provides a directly applicable algorithmic basis for designing delivery paths under building-height and no-fly-zone constraints in this study.

2.5. State of Research on Grid Electricity CO_2 Emission Factors

The grid CO_2 emission factor refers to the indirect carbon dioxide emissions associated with obtaining and consuming one unit of electricity (1 kWh) from the power grid. Government agencies also typically publish national emission factors on a regular basis [52]. In addition, some scholars have projected future emission factors based on historical trends; for example, Cai Bofeng and colleagues projected that provincial grid emission factors in China would decline substantially over 2020–2035, with an average reduction of 43% across provinces [53].

2.6. Status of Research on Carbon Emissions from Low-Altitude Last-Mile Logistics

Existing studies on carbon emissions from UAV last-mile delivery often rely on simplified networks and scenario-based assumptions, rather than explicitly leveraging large-scale real order data, to assess differences in energy use and emissions between UAVs and conventional ground vehicles.

Some studies focus on the full life-cycle carbon footprint of UAVs—from manufacturing and operation to end-of-life recycling [13,23]—but they do not conduct fine-grained last-mile assessments. Other studies examine routine logistics delivery by comparing the carbon emissions of conventional delivery and UAV delivery [24], comparing emissions between truck-based consolidated drop-offs and point-to-point UAV delivery. On the other hand, Figliozzi et al. [23] analyzed emission differences across multiple vehicle types and UAV delivery, Kirschstein et al. [25] compared energy use between a "fixed depot + UAV" system and "truck delivery," and Brown and Bushuev et al. [22] developed a last-mile fleet configuration model.

In summary, although a substantial body of work has examined UAV-related carbon emissions, some studies focus on life-cycle carbon footprints spanning manufacturing, operation, and end-of-life recovery, whereas others develop only simplified energy-consumption models without addressing last-mile delivery. Even studies that explicitly consider carbon emissions from UAV last-mile delivery rarely leverage large volumes of real orders or integrate an assessment framework that combines 3D spatial constraints of representative megacities, established UAV energy-consumption models, per-kilometer energy estimates for electric transport modes, path-planning algorithms, and regional grid carbon-emission factors.

3. Materials and Methods

This study adopts a quantitative, simulation-based comparative case-study design to assess carbon emissions from last-mile parcel delivery by UAVs versus couriers. Taking Shanghai as a case study, we establish a complete evaluation chain encompassing data integration, UAV trajectory generation and its energy-consumption modeling, courier delivery energy modeling, and electricity-to-carbon factor-based carbon-emission accounting, and we propose a reproducible methodological framework termed UCCA (UAV–Courier Carbon Accounting). The overall research-design workflow is shown in Figure 1. This design is appropriate because the research objective is to compare the carbon-emission implications of two delivery modes under real-order demand, urban 3D spatial constraints, and standardized accounting assumptions.

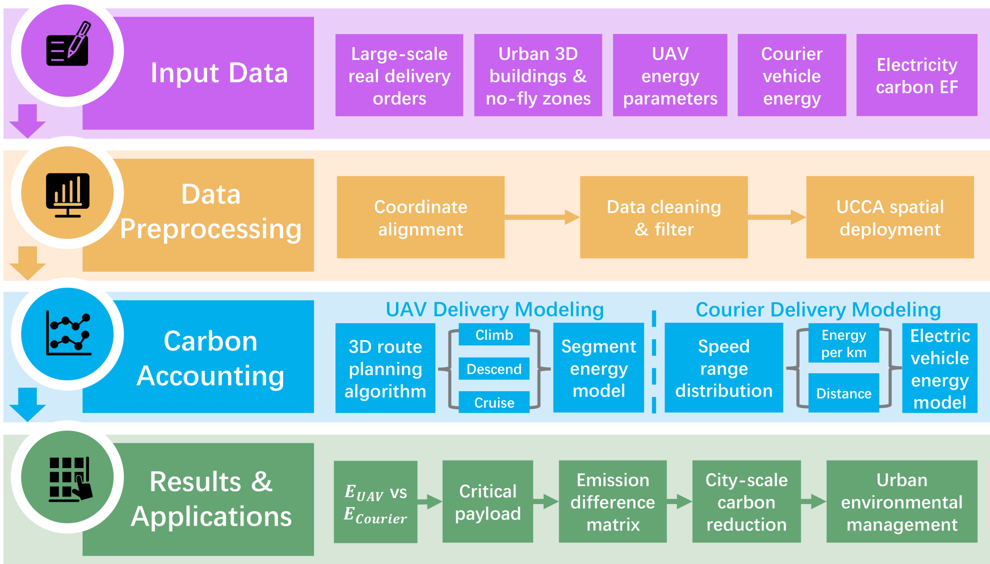

Figure 1. Workflow of the UCCA framework for assessing carbon emissions from urban low-altitude logistics in Shanghai.

First, we integrate order acceptance and delivery locations, station points of interest (POIs), building-height data, no-fly zones, and courier trajectory data to construct the UAV–Courier dataset. We then generate feasible trajectories under 3D urban obstacles and no-fly constraints using a 3D path-planning algorithm based on Sartori et al. [28]; while keeping the electricity-to-carbon factor consistent, we decompose UAV delivery into a two-leg flight: (i) from the parcel acceptance site (the depot hangar) to the delivery point and (ii) from the delivery point to the nearest hangar. Based on an empirically derived mathematical model linking UAV power to speed and flight state, we further decompose UAV energy consumption into three components: ascent, descent, and level-flight cruising. For conventional courier delivery, energy consumption is estimated from the cumulative mileage of high-frequency trajectory data collected over an extended period for a group of Cainiao Network (Cainiao) couriers, together with parcel information linked to these trajectories, yielding the per-parcel delivery cost. We then convert both UAV and courier delivery to a CO_2 emission factor (EF) under the same electricity-to-carbon factor to ensure comparability. Finally, we estimate per-parcel energy use and carbon emissions using the segment-specific power consumption of the UAV across different speed settings and the courier's per-kilometer electricity use at different speeds, and we compute and analyze multiple sets of results.

3.1. Study Area Overview

We select Shanghai's central urban area as the study region, with a focus on the spatial pattern of urban parcel-delivery activities within the built-up area. Shanghai is a municipality directly under the central government of the People's Republic of China and a nationally recognized megacity and global first-tier city, located in eastern China at the mouth of the Yangtze River, covering a total area of 6340.5 km^2 and comprising 16 districts. By the end of 2024, Shanghai's permanent resident population reached 24.8026 million [54]. The dense building stocks and complex transport system of Shanghai provide a representative setting for urban last-mile logistics activities.

Over the past decade, with the rise in e-commerce and the widespread adoption of on-demand delivery services, parcel volumes in Shanghai's urban area have continued to grow rapidly. In 2024, Shanghai handled 4.95 billion parcel deliveries, a year-on-year increase of 27.5%, accounting for 2.8% of China's total parcel volume. Revenue from the express-delivery industry accounted for 34.6% of the national total, ranking first nationwide [55].

According to the Shanghai 14th Five-Year Plan for Green and Low-Carbon Development [26], the urban delivery sector has been identified as a priority area for environmental sustainability transitions. Against this backdrop, both academia and industry urgently require scientific and accurate methods to assess carbon emissions under alternative delivery pathways.

The study area features diverse building types, a dense road network, and highly concentrated residential demand, providing an ideal setting for the UCCA framework developed in this study to conduct comparative carbon-emission assessments for last-mile express parcel delivery.

3.2. Data Sources

This study integrates last-mile express delivery data, urban spatial environment data on buildings and no-fly zones, energy-consumption data for UAVs and courier vehicles, and carbon-emission factor data to support carbon accounting for both UAV-based and courier-based delivery.

3.2.1. UAV Delivery Data

UAV delivery data are used to quantify flight trajectories and energy consumption, among other attributes. This section describes the datasets used for UAV delivery in this study.

1. Building data: These data are derived from the China Multi-Attribute Building (CMAB) vector dataset [56]. It covers 3667 cities across China and includes more than 31 million buildings and 23.6 billion m^2 of rooftops.
2. No-fly zone data (NoFly): UAV no-fly polygons were defined using the "parks and green spaces" category from the OpenSpaceGlobal urban open-space product [57].
3. UAV parcel-delivery data: These data were obtained from the LaDe last-mile express delivery dataset. LaDe covers six consecutive months of Cainiao last-mile logistics data and includes five cities: Shanghai, Hangzhou, Chongqing, Yantai, and Jilin. It contains extensive parcel pickup and drop-off records, partial courier trajectory information, and urban road-network data, involving 21 k couriers and 10,677 k parcels [27].
4. UAV return-to-hangar data: We used the 2025 coordinate dataset of Cainiao stations in Shanghai (CaiNiao_ShangHai2025), which we extracted from Amap (Gaode Map, https://lbs.amap.com, accessed on 18 August 2025) via its open Application Programming Interface (API).
5. Baseline flight altitude for UAV routes: The baseline altitude was derived from civil aviation industry standards of the People's Republic of China. The minimum route-design altitude should be higher than 40 m above the zero-elevation datum, and the maximum should not exceed 120 m above the altitude reference datum [58].
6. Logistics UAV type: The power model in this study is based on field-measured energy-consumption data from the DJI M210 RTK V2 quadrotor UAV (SZ DJI Technology Co., Ltd., Shenzhen, China) [59].
7. Standard curve for payload weight–energy consumption: We adopted the multirotor UAV power model proposed by Gong et al. [40] as the baseline for energy calculations. This model establishes a general three-dimensional power model and provides closed-form power expressions for horizontal flight, vertical ascent, and vertical descent. In particular, the payload–power relationships used in this study are derived from the model-based simulation results reported by Gong et al. [40], rather than from direct

parcel-delivery measurements. We, therefore, treat the resulting UAV estimates as baseline model outputs and explicitly propagate an additional model-form uncertainty in later sections.

3.2.2. Conventional Courier Delivery Data

To construct a carbon-emission model for conventional courier delivery, data on travel distance and the speed distribution during delivery tasks are required. This section describes the datasets used for conventional courier delivery.

1. Courier trajectory data: Derived from the last-mile parcel delivery dataset LaDe [27].
2. Courier parcel data: Derived from the last-mile parcel delivery dataset LaDe [27].
3. Energy-consumption data for courier delivery vehicles: We adopted the cross-vehicle energy-consumption synthesis reported by Weiss et al. [42] in Environmental Sciences Europe. In measuring energy consumption for multiple vehicle types, the study also accounted for a standardized driver body mass of 70 kg, making the estimates more representative of real-world conditions.

In addition, to examine energy use of large electric two- and three-wheelers under different speeds, we referenced Ohde et al. [44], who reported the relationship between average vehicle speed and average battery energy consumption for small urban electric cars. This choice is physically motivated by the shared characteristics of electric drivetrains, including high conversion efficiency, regenerative braking, and the absence of idling losses, which together produce broadly similar speed-related energy-consumption mechanisms across electric vehicle classes [42].

To match the proxy curve to the target vehicle class, we calibrate its magnitude using the real-world average energy-consumption data for larger electric two- and three-wheelers compiled by Weiss et al. [42]. Their dataset explicitly covers larger electric two- and three-wheelers and reports real-world energy-consumption statistics with uncertainty ranges, thereby providing an empirical anchor for the courier baseline used here.

3.2.3. Data for Converting Electricity Use to Carbon Emissions

To consistently convert electricity consumption into greenhouse-gas emissions, this study adopts the grid CO_2 emission factor (EF; unit: kg CO_2/kWh). Most mitigation assessments in urban transport and logistics directly apply current or recent average emission factors; however, UAV logistics systems remain in a pilot stage and are expected to scale up only in the coming years. Under China's "Carbon peaking" and "Carbon neutrality" policy agenda, and considering future adjustments in the energy mix, increasing shares of renewables, and improvements in generation efficiency, we adopt the projected 2030 provincial-level EF for Shanghai reported by Cai et al. in their study of China's regional grid CO_2 emission factors [53], applying it consistently to carbon accounting for both UAV and courier delivery.

3.3. Data Preprocessing

This subsection describes the data-cleaning procedure and the construction of the UCCA deployment space to ensure the accuracy and consistency of subsequent path planning and carbon-emission calculations.

3.3.1. Data Cleaning

The raw data are a Shanghai subset extracted from the LaDe real-world delivery dataset, including fields such as delivery identifiers [27], Global Positioning System (GPS)coordinates of acceptance and delivery points, and timestamps. From the six consecutive months of parcel delivery records for Shanghai provided in LaDe [27], we select the first two months, totaling 204,027 records. We then extract five fields from the original dataset: the package ID, the longitude and latitude of the acceptance point, and the longitude and latitude of the delivery point. Next, we exclude records whose acceptance or delivery locations fall within NoFly areas, as well as records with missing location information, from the analysis. After filtering, 185,673 parcel records remain for estimating the average per-parcel energy consumption of UAV delivery.

In parallel, we remove Cainiao_ShangHai2025 station points located within NoFly areas, yielding a cleaned set of valid UAV return-to-hangar locations. Finally, by matching courier and parcel IDs between UAV parcel-delivery data and courier trajectory data, we identify 98,210 parcels with corresponding trajectory information, and we use these trajectory-linked parcel records as the input data for estimating average per-parcel energy consumption for courier delivery.

3.3.2. Sample Comparability Design Under the Released Data Structure

Because the UAV and courier analyses are based on two released Shanghai data batches of LaDe [27] that were organized differently for privacy protection [27], the two delivery modes cannot be compared on exactly the same raw parcel instances in the full-sample analysis. The UAV parcel batch retains usable parcel coordinates and is, therefore, suitable for 3D route generation in the real urban environment, whereas the courier parcel and trajectory records adopt privacy-preserving transformed coordinates that remain valid for within-dataset distance-based calculations but cannot be directly overlaid with real buildings, no-fly zones, or other geographic layers.

Accordingly, the comparability analysis is restricted to indicators that are directly observable or consistently derivable from both released data batches. In this study, we use three such indicators: parcel-level service duration, parcel-level point-to-point distance, and local parcel density. These indicators jointly capture temporal workload, parcel-scale delivery geometry, and local spatial clustering while remaining analytically valid under the released data structure.

3.3.3. Delineation of the UCCA Deployment Space

To comply with civil aviation industry regulations of the People's Republic of China and to reflect real-world urban flight governance [58], we extract from CMAB the building data [56] for Shanghai with heights between 40 m and 120 m above the zero datum as the built-up-area building inputs for the route-planning algorithm, and we incorporate the spatial vector boundaries of NoFly as no-fly zones for subsequent spatial-constraint checks in path optimization (Figure 2).

3.4. Data Notes

1. For privacy protection, the released Shanghai data used in this study separate parcel records with usable original parcel coordinates from trajectory-enabled courier records with transformed privacy-preserving coordinates [27]. In the UAV-side parcel batch, the acceptance and delivery coordinates can be linked to the real urban 3D environment and are, therefore, suitable for UAV route planning. In the courier-side records, however, the parcel and trajectory coordinates are transformed for privacy protection. These transformed coordinates can still be used for internal distance-based calculations, including parcel-level point-to-point distance and local parcel-density estimation, but they cannot be directly overlaid with real building, no-fly-zone, or other geographic layers. As a result, the full-sample UAV and courier analyses cannot be conducted on exactly the same parcel instances, and the cross-sample comparison must be restricted to variables that are validly supported by both released data batches.

2. We use the courier trajectory information, rather than directly using parcel records, to compute energy consumption for conventional delivery, for the following reasons: (i) Using the parcel acceptance and delivery coordinates as the origin and destination implicitly assumes that conventional delivery involves delivering only one parcel per trip, while in practice, couriers often carry multiple parcels along the same route, so this approach would overestimate energy consumption; (ii) using the parcel acceptance and delivery coordinates as the origin and destination also implies that energy is consumed only when the courier is carrying a parcel, but after completing a delivery, couriers may travel to the next pickup location with an empty vehicle, and this energy use is non-negligible. In summary, it is more reasonable to estimate average per-parcel energy consumption and carbon emissions by quantifying the distribution across speed intervals and combining it with courier-vehicle energy-consumption data at different speeds.

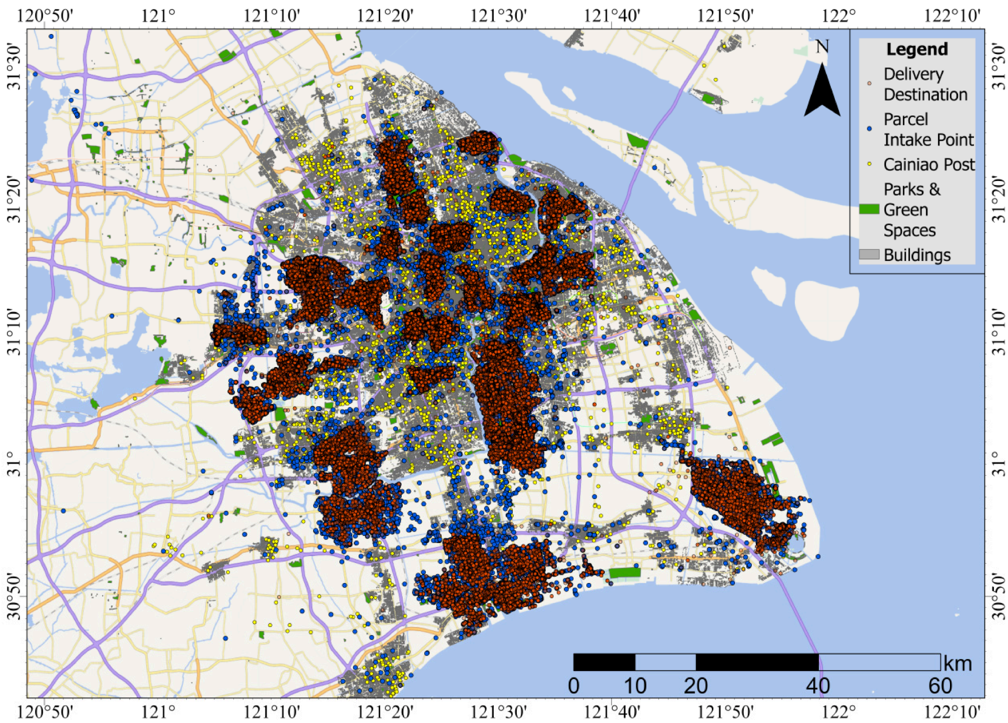

Figure 2. Schematic of the UCCA deployment space.

3.5. UAV Path Planning

Considering heterogeneity in urban building heights and no-fly constraints, we model and compute UAV delivery paths in three-dimensional space. This subsection first introduces the KD-tree method for spatial matching, then describes a 3D path-planning algorithm based on Theta* and Lazy Theta*, and finally presents the specific computational workflow [60]. To improve reproducibility, we report the main implementation settings used in the current MATLAB (vR2020a) workflow, including grid resolution, obstacle filtering, direct-flight screening, and parallel execution strategy.

For each order, we organize UAV operations as a two-leg flight: (i) from the parcel acceptance site (the acceptance-site hangar) to the delivery point and (ii) from the delivery point to the nearest hangar. Due to coordinate errors and related issues, acceptance-site coordinates in real operations exhibit perturbations on the order of tens of meters and are highly clustered around a single station; thus, acceptance sites can be approximated as takeoff hangars. The return hangar is determined via a global nearest-neighbor search to reflect a proximity-based return strategy after delivery.

3.5.1. K-Dimensional Tree Algorithm

A k-dimensional tree (KD-tree) [60] is a space-partitioning tree structure that indexes n points in O (n) space and achieves an average query time of O (log n).

In this study, we insert the filtered CaiNiao_ShangHai2025 coordinates (projected to Web Mercator) into a KD-tree and perform a nearest-neighbor query for each delivery point to identify the closest compliant hangar in space. The procedure is as follows:

1. Build a KD-tree index over station coordinates.
2. For each delivery point, run a nearest-neighbor query to return the coordinates and distance of the nearest hangar.

This approach substantially outperforms brute-force matching that iterates over all station coordinates, achieving O (n log n) efficiency at large sample sizes while ensuring spatially reasonable pairings.

3.5.2. 3D Path Planning Based on Theta* and Lazy Theta*

The approximately optimal 3D route-planning algorithm proposed by Sartori et al. [28], which builds on the Theta* and Lazy Theta* family, was adopted, and its publicly available 3D-grid Theta* implementation was used to generate UAV paths in a 3D grid environment.

Within the UCCA deployment space, buildings and no-fly areas are represented as non-traversable volumes in a local 3D grid, and path planning is performed only after the obstacle field around each origin–destination pair has been spatially cropped and discretized.

3.5.3. Computational Procedure

This subsection details the complete computational workflow for a single UAV delivery task. A representative delivery trajectory and the corresponding 3D environment are shown in Figure 3, and the courier route for the same acceptance and delivery points is shown in Figure 4.

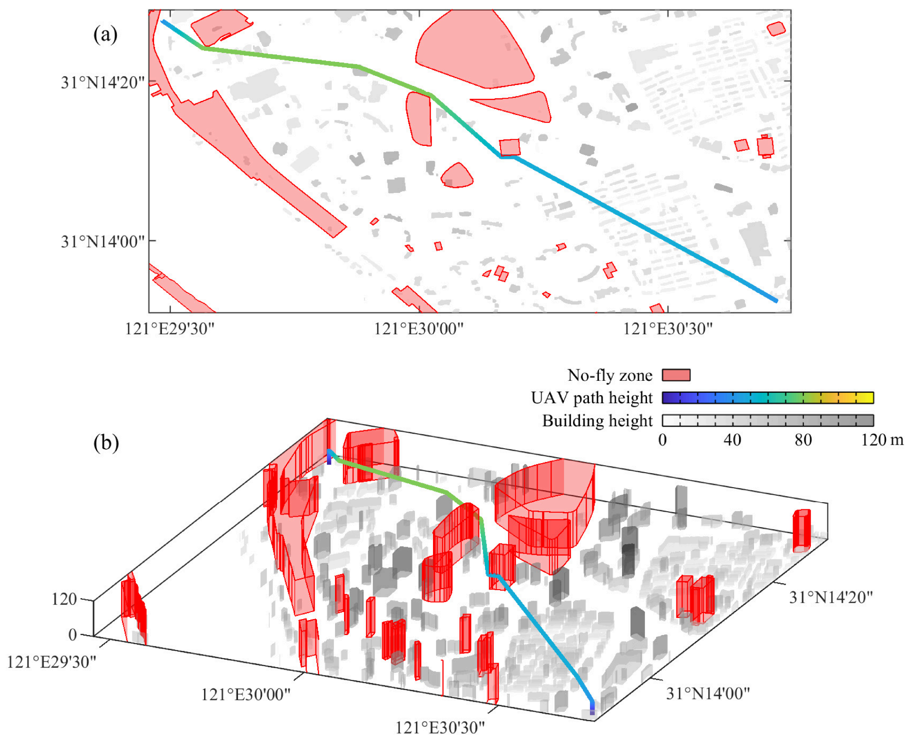

Figure 3. A representative UAV delivery trajectory within the study area in (**a**) 2D and (**b**) 3D views.

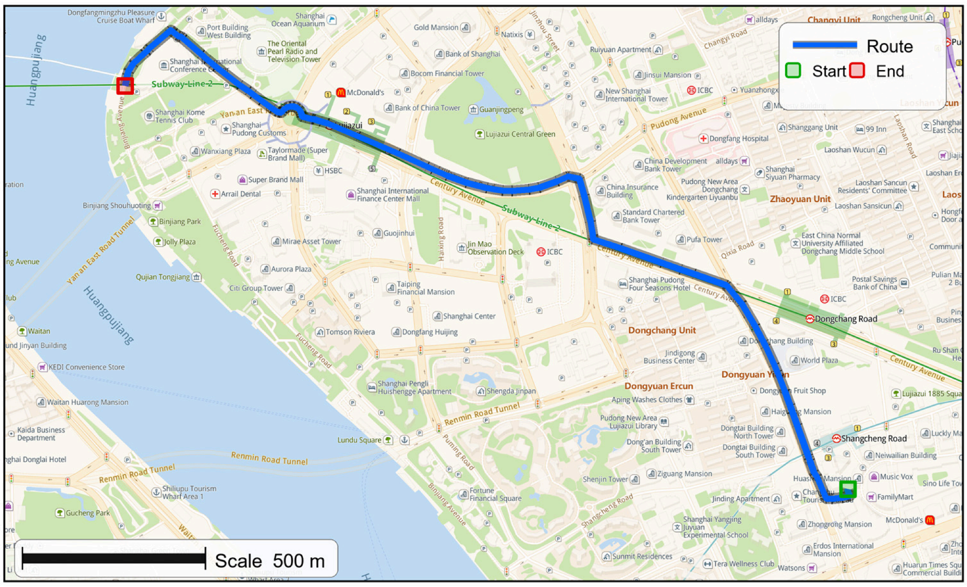

Figure 4. Schematic of a representative delivery route of a conventional courier with the same start and end points as Figure 3.

1. Spatial harmonization and obstacle preparation. Parcel acceptance and delivery coordinates, Cainiao station coordinates from CaiNiao_ShangHai2025, CMAB building-height vectors [56], and NoFly polygons are harmonized to Web Mercator so that all distance calculations and grid operations are performed in a consistent metric coordinate system. Building and no-fly shapefiles are loaded once, and their bounding boxes are precomputed to accelerate spatial filtering.
2. Nearest-hangar matching. We build a KD-tree [60] from the filtered Cainiao station coordinates, and the nearest compliant hangar is queried for each delivery point to determine the destination of the second flight leg.
3. Origin–destination deduplication and caching. To reduce repeated path searches at city scale, origin–destination pairs for both flight legs are hashed and deduplicated on a 10 m grid in Web Mercator space. Orders sharing the same deduplicated key reuse the same path-planning result.
4. Fast corridor screening. Before full 3D search, a local corridor check is performed between the origin and destination. A 200 m corridor buffer is applied around the straight-line segment, and precomputed building/no-fly bounding boxes are used for rapid screening. If no building is above 40 m and no no-fly polygon intersects the corridor, the task is treated as a direct-flight case, and the horizontal distance is calculated directly.
5. Local 3D grid search. If direct flight is not feasible, a local 3D occupancy grid is constructed over the minimum bounding rectangle spanning the start and end points, expanded by 50 m in both horizontal directions and discretized at a 10 m resolution. Building heights are discretized into 10 m vertical layers using ceiling rounding, whereas no-fly polygons are encoded as fully blocked cells up to 120 m (12 layers). The start and end nodes are snapped to the 10 m lattice, and their initial flight layers are set to the larger of the local obstacle layer and the fourth vertical layer (40 m). The outermost x–y boundary and the top/bottom boundary of the local grid are marked as non-traversable. Path search is then performed using a near-optimal any-angle 3D search derived from the Lazy Theta* family [28,51], with 26-neighbor connectivity and line-of-sight relaxation. The line-of-sight test distinguishes full, partial, and blocked visibility. The search cost combines accumulated path cost, a Euclidean-distance

heuristic, and an obstacle-aware penalty term, with the search-weight vector set to [1, 1.25, $||\Delta x, \Delta y, \Delta z||$].

6. Segment extraction. For each feasible path, node-to-node grid differences are converted back to metric distances using the 10 m grid size and decomposed into ascent, descent, and cruise components. Transitions with $|\Delta z| \leq 1$ m are treated as near-horizontal motion. The resulting outputs include vertical ascent/descent distances and their associated horizontal distances for both flight legs, as summarized in Table 1.
7. Parallel execution and batch writing. To improve computational scalability, unique path tasks are dispatched in parallel using a two-queue strategy: all tasks first enter a fast queue and are downgraded to a slow queue if the initial search exceeds a 10 s timeout threshold. At initialization, approximately half of the available workers are assigned to the fast queue and the remainder to the slow queue; once the fast queue is exhausted, all workers are reassigned to the slow queue.

Because the implementation relies only on standard metric inputs—parcel origin, destination coordinates, station coordinates, building polygons with height attributes, and no-fly polygons—the path-planning workflow is transferable to other large cities, provided that equivalent city-specific spatial data are available and can be harmonized into a consistent projected coordinate system.

Table 1. Description of output fields and definitions for UAV delivery path-planning results.

Field	Definition
ID	Primary key
order_id	Parcel order identifier (input order ID).
Climb1_vert	Vertical distance traveled during ascent in leg 1.
Descend1_vert	Vertical distance traveled during descent in leg 1.
Cruise1	Total horizontal-projection length of leg 1.
Climb1_horiz	Cumulative horizontal distance during ascent in leg 1.
Descend1_horiz	Cumulative horizontal distance during descent in leg 1.
Climb2_vert	Vertical distance traveled during ascent in leg 2.
Descend2_vert	Vertical distance traveled during descent in leg 2.
Cruise2	Total horizontal-projection length of leg 2.
Climb2_horiz	Cumulative horizontal distance during ascent in leg 2.
Descend2_horiz	Cumulative horizontal distance during descent in leg 2.

3.6. Speed-Interval Distribution of Couriers

To estimate the distance traveled by couriers over each trajectory segment while completing delivery tasks in practice, we compile statistics for all trajectory segments associated with the 98,210 parcels that have trajectory information. The procedure is as follows:

1. Coordinate distance calculation: For each trajectory, the distance between adjacent points is computed using the 2D Euclidean formula:

$$d = \sqrt{(x_{i+1} - x_i)^2 + (y_{i+1} - y_i)^2} \tag{1}$$

2. Outlier removal: First, due to positioning errors, some inter-point distances may be abnormal; considering the upper speed bound of courier vehicles, we set a threshold of 1000 m and discard any single-segment distance exceeding this threshold to remove

obvious noise that would distort total distance estimates; second, to account for parking or non-working periods, if a courier's trajectory coordinates remain unchanged for an extended duration, the segment is treated as abnormal, and given that red-light durations in cities are typically 60–120 s, we set the threshold to six intervals (120 s). Segments remaining after outlier removal are treated as valid intervals.

3. Speed-interval distribution statistics: Each pair of adjacent trajectory points is treated as one interval; we compute the travel distance d_i for each valid interval i to estimate the average speed v_i for that interval and store the results as interval–speed data.

3.7. The UCCA Carbon-Emission Model

Building on the path-planning results and the analysis of delivery-behavior characteristics, we further develop a unified carbon-accounting framework, termed the UAV–Courier Carbon Accounting (UCCA) model. This subsection describes the overall structure of the UCCA model and details the carbon-emission calculation methods for different delivery modes.

3.7.1. UAV Delivery Carbon-Emission Model E_{UAV}

We develop the UAV delivery carbon-emission model E_{UAV} using the multirotor UAV power model proposed by Gong et al. [40] as the baseline for energy estimation. That study provides level-flight power $P_f(w)$, vertical-ascent power $P_a(w)$, and vertical-descent power $P_d(w)$ (in W) as functions of UAV payload w(kg) and further constructs a total power model for steady-state 3D flight. Their experiments, conducted with a DJI M210 RTK V2, collected data over speed of $V_f(level\ flight)$, $V_a(ascent)$, $V_d(descent)$, fitting power–speed curves and the "energy per unit distance–speed" relationship that can serve as an energy benchmark for UAV last-mile delivery.

When evaluating the parent 3D model against measured UAV power in arbitrary steady 3D flight, Gong et al. [40] reported an average relative difference of 13.20%. In this study, we, therefore, use ±13.2% as a pragmatic model-form uncertainty range to expand the uncertainty interval of UAV energy and carbon estimates. This uncertainty proxy is interpreted as an aggregate representation of the gap between idealized model predictions and real operations.

Based on measurements and linear regression, the steady-state power–payload (W–kg) relationships for the three flight modes are expressed with payload w as the independent variable:

$$P_a(w) = a_a + b_a w \tag{2}$$

$$P_f(w) = a_f + b_f w \tag{3}$$

$$P_d(w) = a_d + b_d w \tag{4}$$

These correspond to level flight (forward), vertical ascent, and vertical descent, respectively. For each speed setting (V_f,V_a,V_d), each delivery trajectory is decomposed into ascent height gain $h_\uparrow$(m), level-flight distance c(m), and descent height loss $h_\downarrow$(m). Under steady speeds, the three segment-wise energies (J) for a single parcel are:

$$E_\uparrow(w) = \frac{P_a(w)}{V_a} h_\uparrow \tag{5}$$

$$E_\rightarrow(w) = \frac{P_f(w)}{V_f} c \tag{6}$$

$$E_\downarrow(w) = \frac{P_d(w)}{V_d} h_\downarrow \tag{7}$$

The total energy $E(w)$ (J) is, therefore:

$$E(w) = \frac{P_a(w)}{V_a} h_{\uparrow} + \frac{P_f(w)}{V_f} c + \frac{P_d(w)}{V_d} h_{\downarrow} \tag{8}$$

Combined with the electricity-related carbon emission factor EF (kg/kWh), the estimated carbon emissions per trajectory E_{UAV}(kg) are:

$$E_{\mathrm{UAV}}(w) = \frac{E(w) \cdot \mathrm{EF}}{3.6 \times 10^6} \tag{9}$$

3.7.2. Carbon-Emission Model for Conventional Courier Delivery E_{Courier}

The conventional courier delivery carbon-emission model E_{Courier} quantifies the carbon emissions of a single delivery task based on travel distance, speed intervals, and the corresponding energy-consumption parameters. Because parcel-level direct energy measurements for Shanghai courier vehicles are unavailable, the courier baseline is formulated here as a proxy-based calibrated model rather than a direct measurement model. For computational simplicity, we ignore the effect of mass differences attributable to a single parcel relative to the courier and vehicle body on energy consumption. For parcel delivery, we have computed the average speed (km/h) and segment distance (km) for each valid interval. The dataset contains M parcels, and within the N valid intervals in the corresponding courier trajectory data, the i-th valid interval has distance d_i (km) and average speed v_i(km/h).

As shown in Figure 5, certified energy consumption across multiple classes of electric road vehicles generally increases with vehicle mass [42]. The pooled regression line is intended only to visualize the overall cross-class tendency, while the class-specific patterns remain heterogeneous. This cross-vehicle regularity supports the use of a shape-calibrated proxy for the courier baseline when parcel-level direct energy measurements are unavailable.

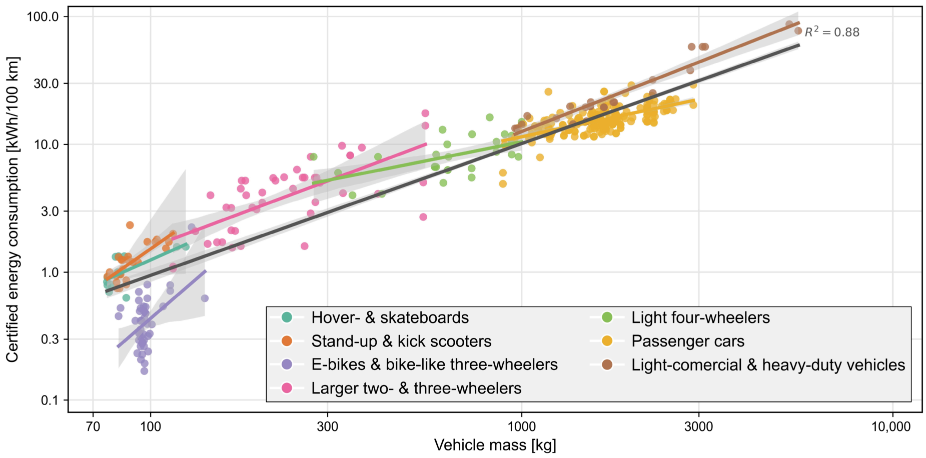

Figure 5. Redrawn cross-vehicle relationship between certified energy consumption and vehicle mass across electric road-vehicle classes. Redrawn and adapted from Weiss et al. [42], licensed under CC BY 4.0. The grey shaded areas denote the 95% uncertainty intervals for the regression lines of uncertainty.

Combining (i) the per-distance energy consumption of large electric vehicles E_s (Wh/km) from the cross-vehicle compilation by Weiss et al. [42], (ii) the experimentally measured relationship between average speed (km/h) and battery energy consumption per km (Wh/km) $E_0(v)$, and its full-speed-domain mean E_c reported by Ohde et al. [44], we apply a scaling factor β to obtain the speed (km/h)–battery energy consumption (Wh/km) function $E(v)$ for large electric two- and three-wheelers and use the medium- to long-term projected provincial grid emission factor EF(kg/kWh) [53] to estimate per-parcel carbon emissions $E_{Courier}$ as:

$$E_{Courier} = \frac{1}{M} \times \sum_{i=1}^{N} \frac{E(v_i)}{1000} \cdot d_i \cdot EF \tag{10}$$

Here, the speed (km/h)–battery energy consumption (Wh/km) relationship for large electric vehicles E(v) is:

$$E(\mathrm{v}) = \frac{E_0(v)}{\beta} \tag{11}$$

The scaling factor β is obtained via calibration to ensure that the mean energy-consumption level of the scaled model is consistent with the two-/three-wheeler baseline:

$$\beta = \frac{E_c}{E_s} \tag{12}$$

To assess the impact of this simplifying assumption, we analyze it in the sensitivity analysis and further evaluate three alternative specifications in Section 4.3: a lower-bound curve, a mean curve, and an upper-bound curve based on the uncertainty range reported by Weiss et al. [42].

4. Results

Based on the UCCA framework described above, this section systematically analyzes carbon-emission outcomes for UAV delivery and conventional courier delivery.

4.1. Observable Comparability Between the UAV Valid Parcel Sample and the Courier Parcel Sample

Because the UAV and courier analyses rely on different released LaDe data batches, we assessed their comparability using three shared observable indicators: parcel-level service duration, point-to-point distance, and local parcel density.

As shown in Figure 6 and Table 2, the two samples are broadly comparable across all three dimensions. The service-duration distributions are similar overall, although the UAV parcel sample shows a somewhat longer right tail (mean/median: 118.68/79.00 min for the UAV sample versus 94.38/71.00 min for the courier sample). The point-to-point distance distributions are highly similar, with nearly identical mean distances (2.10 km versus 2.09 km) and comparable medians (1.62 km versus 1.78 km). The two samples also exhibit similar local parcel densities at the 1 km, 5 km, and 10 km scales, indicating broadly comparable levels of local order concentration.

Taken together, these results suggest that the UAV parcel sample and the trajectory-linked courier parcel sample are broadly comparable in their observable temporal, geometric, and local clustering characteristics.

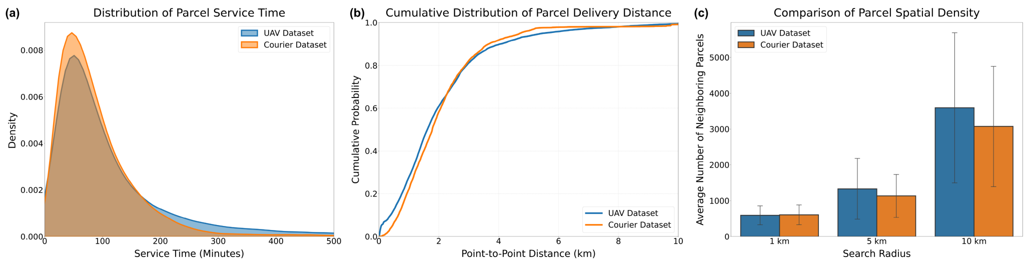

Figure 6. (**a**) Distribution of parcel service time. (**b**) Cumulative distribution of parcel point-to-point distance. (**c**) Comparison of local parcel density.

Table 2. Statistical comparison of three shared observable indicators between the UAV parcel sample and the trajectory-linked courier parcel sample.

Indicator	UAV Valid Parcel Sample (n = 185,673)	Courier Parcel Sample (n = 98,210)	Interpretation
Service duration	118.68 min (median 79.00)	94.38 min (median 71.00)	Similar right-skewed workload structure
Point-to-point distance	2.10 km (median 1.62)	2.09 km (median 1.78)	Highly similar parcel-scale delivery geometry
Local parcel density within 1 km	592.9	606.9	Similar local clustering
Local parcel density within 5 km	1331.7	1134.5	Similar intermediate-scale clustering
Local parcel density within 10 km	3592.2	3073.3	Similar large-scale clustering

4.2. Results of the UAV Delivery Carbon-Emission Model E_{UAV}

4.2.1. Sample Composition and Validity

Using the May–June orders from the Shanghai subset of the LaDe dataset as the full population (204,027 records), we obtain 185,673 valid samples (91.00%) after consistent projection and spatial cleaning; all valid samples are mapped to a unified projection and the same UCCA deployment space (Table 3).

Table 3. Data cleaning and validity statistics for two months of Shanghai LaDe orders.

Category	Count	Share
Total records of the Shanghai LaDe dataset	204,027	100%
Valid records	185,673	91.00%
Invalid 1: within no-fly zones	16,085	7.88%
Invalid 2: local grid-construction or path-search failure	2189	1.07%
Invalid 3: missing coordinates in the LaDe dataset	80	0.04%

To further characterize Invalid 2, we conducted a preliminary diagnostic analysis on a large subset of unresolved origin–destination pairs. Most cases were associated with leg-1 (84.2%) or leg-2 (13.0%) grid-construction failures, whereas endpoint blocking after rasterization accounted for only a minor share (2.6% for leg 1). These findings indicate that Invalid 2 primarily arose from locally complex spatial configurations around specific delivery tasks, rather than from general instability of the underlying path-planning algorithm.

4.2.2. UAV Path-Planning Results

Under the UCCA two-leg flight setting, we decompose each trajectory into three segments: ascent (cumulative vertical gain $h_{\uparrow}$), cruising (horizontal projected distance c), and descent (cumulative vertical loss $h_{\downarrow}$). We summarize the valid samples and, after aggregating the two legs, obtain the per-parcel mean values (including an additional +40 m for takeoff and −40 m for landing) (Table 4):

$$\mathrm{h}_{\uparrow} = 88.4475\ \mathrm{m},\ \mathrm{h}_{\downarrow} = 88.4023\ \mathrm{m},\ \mathrm{c} = 3122.2016\ \mathrm{m} \quad (13)$$

Table 4. Segment-wise distance statistics for representative UAV delivery tasks (m).

Metric	Sum	Mean	Max
Climb_vert	16,422,310	88.447485	400
Descend_vert	16,413,920	88.402299	410
Cruise	579,708,538.5	3122.201605	78,173.390577
Climb_horiz	38,168,320.098	205.567423	38,819.043
Descend_horiz	63,851,072.875	343.8899	44,452.025

4.2.3. UAV Delivery Energy Use and Carbon Emissions

Gong et al. [40] experimentally calibrated the DJI M210 RTK V2 platform and established empirical power–payload–velocity functions for three flight regimes: forward flight at 0–15 m/s, ascent at 0–5 m/s, and descent at 0–3 m/s.

For practical implementation, we discretize speeds into six levels. The idealized payload (kg)–energy consumption (Wh) relationship for each speed setting is shown in Figure 7. The baseline average energy consumption (Wh) per single delivery as a function of parcel payload (kg) across the six UAV speed settings is reported in Table 5. The baseline payload (kg)–carbon emissions (kg) table for a single UAV delivery across the six speed settings is provided in Table 6. The payload–energy plot and the payload–carbon-emission functions for a single delivery across the six speed settings are shown in Figures 8 and 9.

$$\mathrm{V1} : (\mathrm{V_f}, \mathrm{V_a}, \mathrm{V_d}) = (3.0, 1.0, 0.5)\mathrm{m/s} \tag{14}$$

$$\mathrm{V2} : (\mathrm{V_f}, \mathrm{V_a}, \mathrm{V_d}) = (3.0, 2.0, 1.0)\mathrm{m/s} \tag{15}$$

$$\mathrm{V3} : (\mathrm{V_f}, \mathrm{V_a}, \mathrm{V_d}) = (6.0, 3.0, 1.5)\mathrm{m/s} \tag{16}$$

$$\mathrm{V4} : (\mathrm{V_f}, \mathrm{V_a}, \mathrm{V_d}) = (9.0, 4.0, 2.0)\mathrm{m/s} \tag{17}$$

$$\mathrm{V5} : (\mathrm{V_f}, \mathrm{V_a}, \mathrm{V_d}) = (12.0, 5.0, 2.5)\mathrm{m/s} \tag{18}$$

$$\mathrm{V6} : (\mathrm{V_f}, \mathrm{V_a}, \mathrm{V_d}) = (15.0, 6.0, 3.0)\mathrm{m/s} \tag{19}$$

Table 5. Baseline * load–average energy consumption matrix (Wh) for a single UAV delivery across speed settings.

Speed_Bin	1 kg	2 kg	5 kg	8 kg	10 kg
V1	83.1	121.3	235.9	350.5	426.9
V2	72.8	106.2	206.4	306.6	373.4
V3	38.0	54.9	105.9	156.9	190.9
V4	26.6	37.8	71.4	105.0	127.4
V5	21.8	30.1	55.1	80.1	96.7
V6	19.9	26.6	46.6	66.5	79.9

* The values in Table 5 are baseline estimates. The corresponding uncertainty interval in Figure 8 was derived from the average relative difference reported for the underlying 3D UAV power model in Gong et al. [40].

Table 6. Baseline * load–carbon emissions matrix (kg CO_2) for a single UAV delivery across speed settings.

Speed_Bin	1 kg	2 kg	5 kg	8 kg	10 kg
V1	0.027	0.039	0.077	0.114	0.139
V2	0.024	0.035	0.067	0.100	0.121

Table 6. *Cont.*

Speed_Bin	1 kg	2 kg	5 kg	8 kg	10 kg
V3	0.012	0.018	0.034	0.051	0.062
V4	0.009	0.012	0.023	0.034	0.041
V5	0.007	0.010	0.018	0.026	0.031
V6	0.006	0.009	0.015	0.022	0.026

* The values in Table 6 are baseline mean estimates. The corresponding uncertainty interval in Figure 9 was derived from the average relative difference reported for the underlying 3D UAV power model in Gong et al. [40].

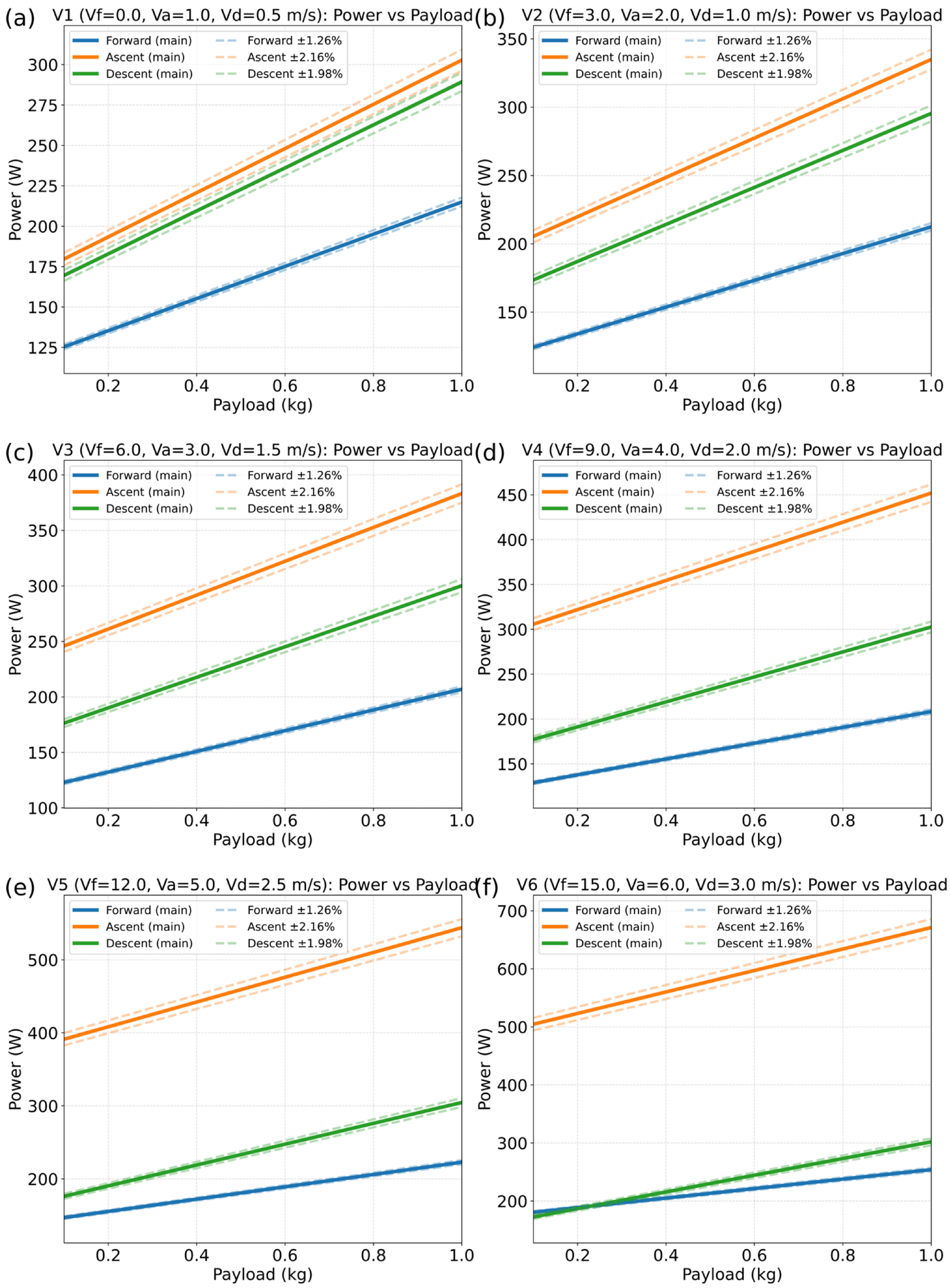

Figure 7. Ideal power–payload relationships for ascent/descent/level flight across six UAV speed settings. Panels (**a**–**f**) correspond to speed settings V1–V6; each panel shows power–payload curves for level flight (Forward), ascent (Ascent), and descent (Descent); dashed lines indicate uncertainty ranges, reflecting the influence of parameter variability in the power model.

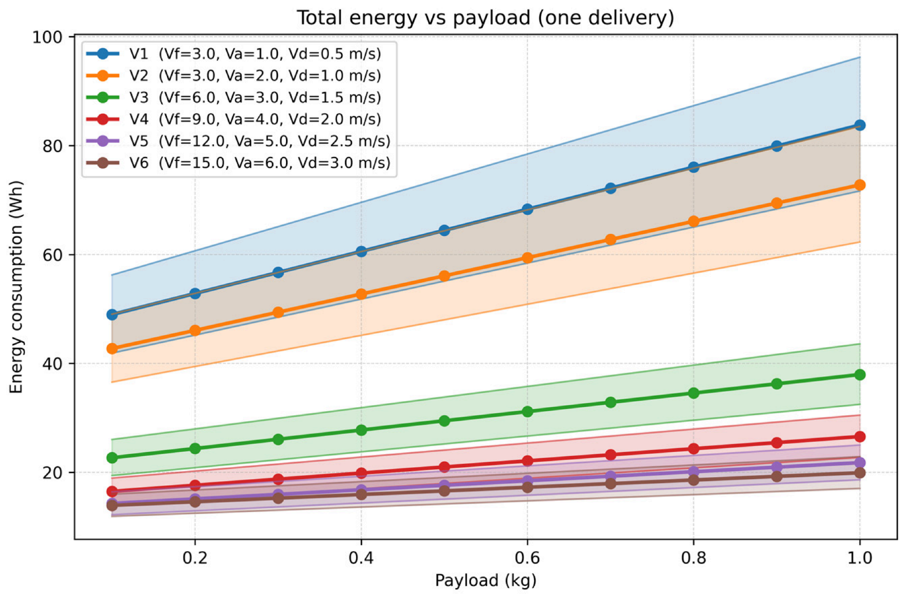

Figure 8. Relationship between total UAV energy consumption and parcel payload in a single delivery task. Curves correspond to speed settings V1–V6; upper and lower bounds (represented by colored shadows) indicate the uncertainty interval after propagating model uncertainty.

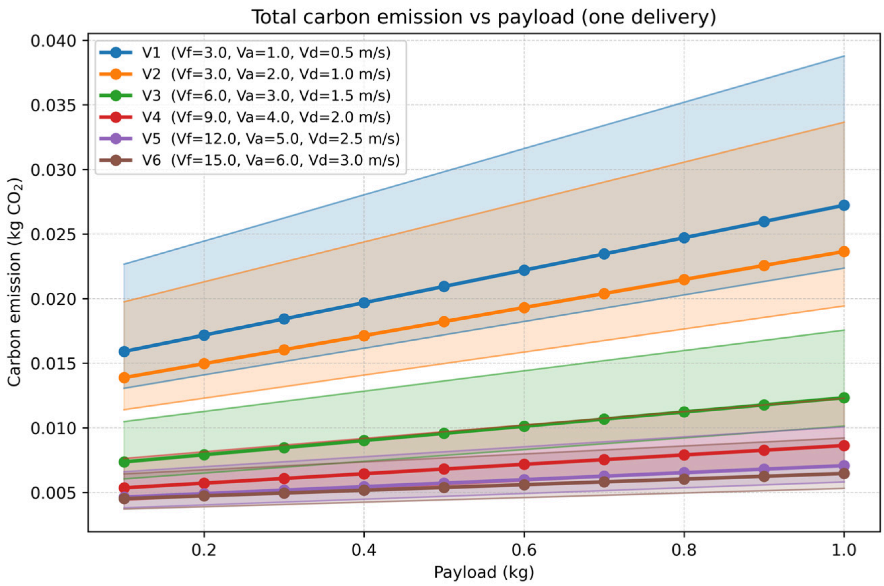

Figure 9. Relationship between total UAV carbon emissions and parcel payload in a single delivery task. Curves correspond to speed settings V1–V6; the colored shadows represent the uncertainty intervals for each respective speed setting, reflecting the influence of power-model and parameter variability on emission estimates.

Within the modeled steady-flight framework used in this study, higher speed settings are associated with lower estimated per-parcel carbon intensity because the reduction in task duration offsets the increase in power per unit time at higher speeds. This relationship should not be interpreted as a universal operational rule. In practice, UAV speed is constrained by regulation, safety requirements, maneuverability, hovering demand, and energy-reserve considerations, all of which may modify the observed speed–emission relationship. When comparing across payloads (1–10 kg) at a fixed speed setting, emissions increase approximately linearly with payload, and the slope is smaller under higher modeled speed settings.

4.3. Results of the Courier Delivery Carbon-Emission Model $E_{Courier}$

4.3.1. Results of Speed-Interval Distribution for Couriers

From 5,590,332 trajectory-record intervals, after removing outliers where adjacent points are more than 1 km apart and intervals in which the position remains unchanged for six consecutive segments, we obtain 3,413,556 valid intervals and derive the overall speed distribution across these valid intervals (Figure 10).

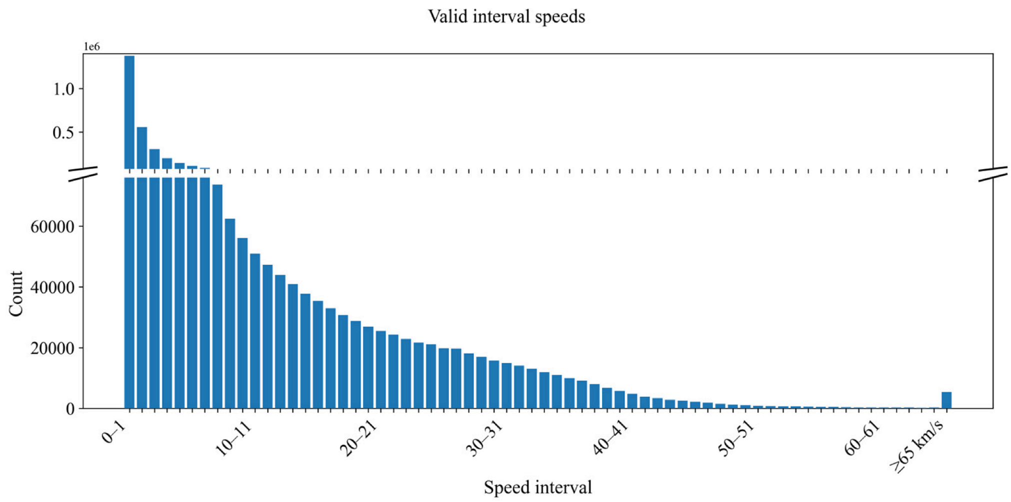

Figure 10. Speed distribution of valid trajectory intervals for couriers. The x-axis shows speed bins (km/h), and the y-axis shows interval counts; a broken axis is used to simultaneously display high-frequency low-speed intervals and the long-tailed high-speed intervals.

Couriers primarily travel at low to medium speeds during delivery, with high speeds ($\geq$65 km/h) accounting for only a small fraction. Moreover, due to behaviors such as delivery activities and loading/unloading, vehicles stop and start frequently, resulting in a high share of low-speed intervals in the 0–10 km/h range.

4.3.2. Courier Delivery Energy Use and Carbon Emissions

To quantify the speed–energy relationship of large electric courier vehicles, we first refer to the cross-vehicle energy compilation by Weiss et al. [42] for the mean per-distance energy consumption E_s(kWh/km) of large electric two- and three-wheelers:

$$\mathrm{Es} = 0.093\ (\mathrm{range}: 0.060\text{–}0.135) \tag{20}$$

We also adopt the relationship between average speed and average battery energy consumption for electric cars $E_{\mathrm{EV}}(v)$ reported by Ohde et al. [44] across many brands and models, from which the full-speed-domain mean E_c(kWh/km) is:

$$\mathrm{Ec} = 0.15307 \tag{21}$$

This yields the scaling coefficient β:

$$\beta = \frac{E_c}{E_s} = 1.646\ (range: 1.134\text{–}2.551) \tag{22}$$

We then scale the EV curve downward by a factor of β to obtain the per-kilometer energy-consumption–speed relationship for large electric courier two- and three-wheelers. The speed–energy-consumption-per-kilometer curve is shown in Figure 11:

$$E(v) = \frac{E_0(v)}{\beta} \tag{23}$$

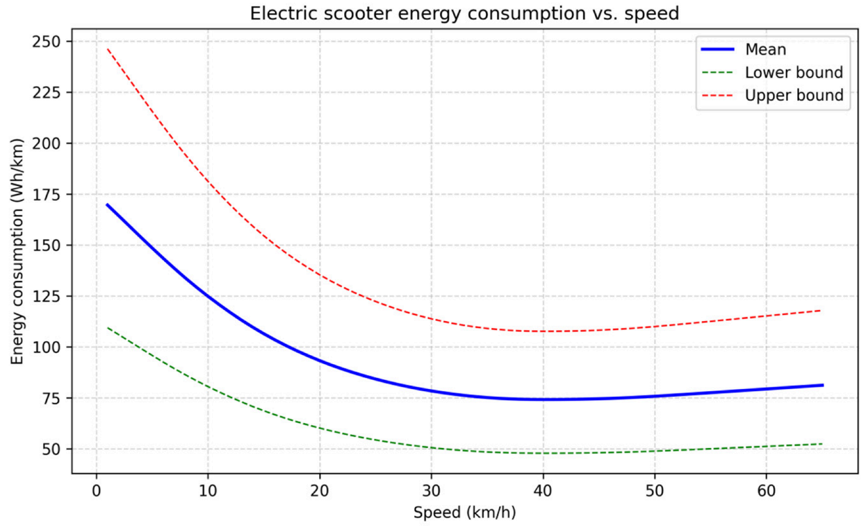

Figure 11. Speed–energy-consumption curve for large electric courier vehicles. The solid line indicates the mean energy-consumption curve, and the dashed lines represent the uncertainty interval.

Specifically, energy use is elevated at low speeds (below 10–15 km/h) due to frequent stop-and-go behavior, prolonged travel time, and inefficient operation. A minimum in energy use and carbon emissions occurs at approximately 40 km/h, after which energy use increases again in the high-speed regime as power demand and aerodynamic/rolling resistance rise.

We adopt the projected medium- to long-term provincial grid emission factor EF (kg/kWh) [53]:

$$\mathrm{EF} = 0.325\ (\mathrm{range}:\ 0.312\text{–}0.432) \tag{24}$$

Combining the expression for per-parcel carbon emissions E_{Courier}(kg):

$$\mathrm{E}_{\mathrm{Courier}} = \frac{1}{M} \times \sum_{i=1}^{N} \frac{E(v_i)}{1000} \cdot d_i \cdot EF \tag{25}$$

We obtain an average per-parcel carbon emission of $\mathrm{E}_{\mathrm{Courier}}$ as follows:

$$\mathrm{E}_{\mathrm{Courier}} = 0.04874\ (\mathrm{range}: 0.03019\text{–}0.09405) \tag{26}$$

5. Discussion

Building on the quantitative results, we discuss the emission differences between UAV and courier delivery, critical thresholds under different payload conditions, and sources of uncertainty in the model, thereby deepening the interpretation of our findings and providing theoretical and data support for practical applications.

5.1. Comparison and Analysis of E_{UAV} and $E_{Courier}$

This subsection conducts a quantitative comparison between E_{UAV} and E_{Courier} at the level of a single delivery task and investigates the underlying drivers in light of delivery characteristics. To examine differences in average per-parcel carbon emissions between UAV delivery and conventional courier delivery under different speed settings, we follow the multirotor UAV power model proposed by Gong et al. [40] and select three UAV speed levels: low (V2), medium (V4), and high (V6):

$$\mathrm{V2}: (\mathrm{V_f}, \mathrm{V_a}, \mathrm{V_d}) = (3.0, 2.0, 1.0)\mathrm{m/s} \tag{27}$$

$$\mathrm{V4}: (\mathrm{V_f}, \mathrm{V_a}, \mathrm{V_d}) = (9.0, 4.0, 2.0)\mathrm{m/s} \tag{28}$$

$$\mathrm{V6}:(\mathrm{V_f},\mathrm{V_a},\mathrm{V_d})=(15.0,6.0,3.0)\mathrm{m/s} \quad (29)$$

In addition, based on the cross-vehicle energy-consumption compilation by Weiss et al. [42], we estimate the carbon emissions for large electric courier-vehicle delivery as:

$$\mathrm{E_{Courier}}=0.04874\ (\mathrm{range}:0.03019\text{–}0.09405) \quad (30)$$

Within the modeled setting adopted here, the estimated UAV emissions decrease with higher speed settings, i.e., $V6 < V4 < V2$. By neglecting the parcel mass—which is negligible relative to the vehicle mass and the courier's body mass—we assume that courier emissions are independent of parcel payload, yielding a constant per-parcel emission level (Figure 12).

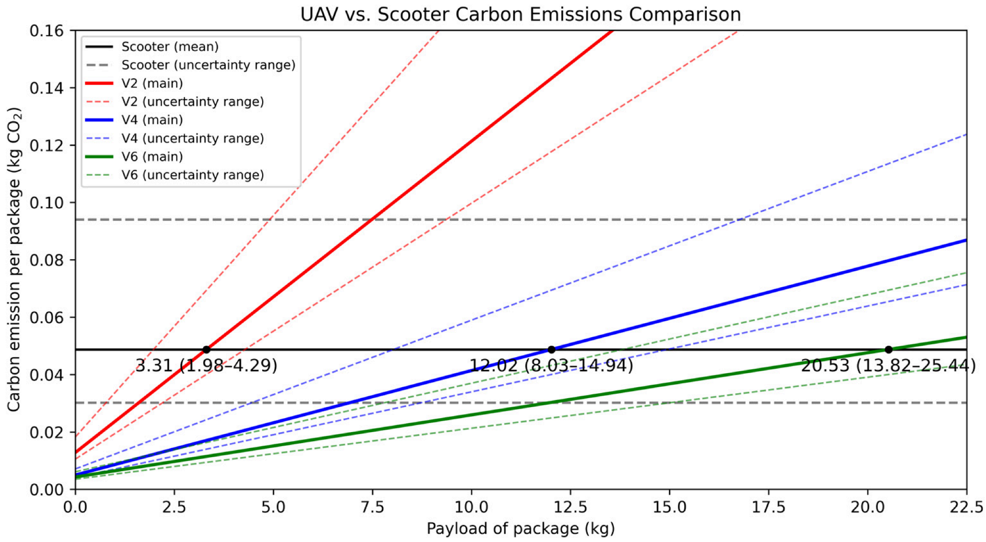

Figure 12. Comparison of per-parcel carbon emissions between UAV and conventional courier delivery under different payloads and the corresponding critical payload. The figure presents the emission curves (with uncertainty bands) for UAV delivery at three representative speed settings (V2/V4/V6), together with the mean courier level and its uncertainty range; the intersections are labeled as "critical payloads," delineating payload ranges in which UAV delivery is relatively lower carbon.

As payload w increases, E_{UAV} rises approximately linearly and intersects the courier baseline sequentially across speed settings, producing critical payload thresholds at which E_{UAV} becomes lower than $E_{Courier}$. To the left of an intersection point, UAV delivery is lower carbon, whereas to the right, courier delivery is lower carbon.

5.2. Critical Payload

We further identify key factors that drive the switching point in relative performance between the two modes. Among these factors, UAV payload has a pronounced impact on energy use and carbon emissions. We define the concept of "critical payload" as the threshold at which the carbon-emission advantage shifts between the two delivery modes under different load conditions. For each "UAV speed bin × courier level" pairing, we compute the intersection point of the emission curves, which is taken as the critical payload (Table 7).

In the heavy-payload regime, UAV emissions increase relatively rapidly with payload, and UAV delivery does not exhibit a carbon-reduction advantage. In the light-payload regime, considering only the mean per-parcel delivery distance, UAV delivery tends to provide greater carbon-reduction potential. As payload increases, the UAV curve rises approximately linearly, and emissions progressively exceed those of couriers.

Table 7. Critical payloads corresponding to intersections between UAV and courier emission curves.

UAV_Bin	Scooter_Curve	Payload_kg	CO_2_kg_Per_Delivery
UAV_V1	Scooter mean	2.711 (1.556–3.556)	0.048742
UAV_V2	Scooter mean	3.312 (1.976–4.285)	0.048742
UAV_V3	Scooter mean	7.593 (4.967–9.512)	0.048742
UAV_V4	Scooter mean	12.019 (8.031–14.935)	0.048742
UAV_V5	Scooter mean	16.393 (11.027–20.322)	0.048742
UAV_V6	Scooter mean	20.525 (13.816–25.440)	0.048742

5.3. Carbon-Emission Difference Matrix

To more intuitively present the carbon-emission differences between UAV and courier delivery across scenarios and to support operational decision-making, we further construct a carbon-emission difference matrix. By computing the emission difference between E_{UAV} and E_{Courier} under varying distance and payload conditions, the matrix clearly delineates the low-carbon advantage regions of different delivery options:

$$\Delta C(\mathrm{w}) = \mathrm{E}_{\text{Courier}} - \mathrm{E}_{\text{UAV}}(w), \tag{31}$$

$\Delta C > 0$ indicates that UAV delivery is lower carbon, whereas $\Delta C < 0$ indicates that courier delivery is lower carbon (Table 8). The matrix can be directly used to formulate operational rules for payload-allocation thresholds. Under a given speed strategy and payload distribution, assigning payload intervals with positive ΔC to UAVs and intervals with negative ΔC to couriers enables a piecewise optimization of carbon-reduction performance.

Table 8. Carbon-emission difference matrix between UAV and courier delivery, with uncertainty intervals.

UAV_Bin_vs_Scooter_Curve	1 kg	2 kg	5 kg	10 kg
UAV_V1-Scooter mean	0.0215 (0.0100–0.0264) kg	0.0089 (−0.0079–0.0161) kg	−0.0288 (−0.0617–0.0149) kg	−0.0916 (−0.1512–0.0665) kg
UAV_V2-Scooter mean	0.0251 (0.0151–0.0293) kg	0.0142 (−0.0004–0.0204) kg	−0.0183 (−0.0467–0.0064) kg	−0.0726 (−0.1239–0.0510) kg
UAV_V3-Scooter mean	0.0364 (0.0312–0.0386) kg	0.0309 (0.0233–0.0341) kg	0.0143 (−0.0003–0.0205) kg	−0.0133 (−0.0396–0.0022) kg
UAV_V4-Scooter mean	0.0401 (0.0364–0.0417) kg	0.0365 (0.0313–0.0387) kg	0.0255 (0.0157–0.0297) kg	0.0073 (−0.0102–0.0148) kg
UAV_V5-Scooter mean	0.0417 (0.0387–0.0429) kg	0.0390 (0.0348–0.0407) kg	0.0308 (0.0232–0.0340) kg	0.0173 (0.0040–0.0229) kg
UAV_V6-Scooter mean	0.0423 (0.0395–0.0434) kg	0.0401 (0.0364–0.0417) kg	0.0336 (0.0272–0.0363) kg	0.0228 (0.0118–0.0274) kg

5.4. Scenario Analysis of Potential Carbon Reduction in Shanghai by 2030

This is a representative Shanghai 2030 scenario rather than a precise forecast. Owing to the lack of parcel-weight distribution data, it should be interpreted as an indication of scale only. Based on the computed carbon-emission difference matrix, we further estimate the potential annual carbon reductions that UAV delivery could achieve in Shanghai in 2030. We define the annual carbon reduction achieved by UAV delivery in 2030, ΔCO_2^{2030}(t), as:

$$\Delta \mathrm{CO}_2^{2030} = \frac{1}{1000}\sum_{\mathrm{w}}[\mathrm{N}_{2030}(w)\cdot\Delta \mathrm{C}(w)] \tag{32}$$

https://doi.org/10.3390/drones10050364

Here, $N_{2030}(w)$ denotes the number of parcels with weight w (kg) in Shanghai in 2030, and $\Delta C(w)$ represents the per-parcel emission difference (kg) between UAV delivery and conventional ground courier-vehicle delivery at the same weight. Because publicly available statistics on parcel-weight distributions at the Shanghai or national scale are currently lacking, we follow Kang et al. [61] and assume an average parcel weight (including goods and packaging) of approximately 1 kg; combined with Shanghai's annual express volume in 2024 ($N_{2024} = 4.95$ billion parcels) and the compound annual growth rate (CAGR) over the past five years [55], we project the 2030 express volume N_{2030} as:

$$\mathrm{N}_{2030} = \mathrm{N}_{2024} \times (1 + CAGR)^{2030-2024} \tag{33}$$

The CAGR is defined as:

$$CAGR = \left(\frac{\mathrm{N}_{2024}}{\mathrm{N}_{2019}}\right)^{\frac{1}{2024-2019}} - 1 \tag{34}$$

This yields CAGR $= 9.56\%$ and a projected $N_{2030} = 8.56$ billion parcels. We then use the weight–emission function for the medium UAV speed setting (V4) together with the mean emission level of ground courier vehicles to obtain the per-parcel carbon reduction ΔC(kg) as:

$$\Delta C(w = 1\text{kg}) = 0.040109\text{kg } CO_2/parcel \tag{35}$$

$$(range : 0.036447\text{kg } CO_2/\text{parcel–}0.041653\text{kg } CO_2/\text{parcel})$$

Under the above assumptions, substituting into the ΔCO_2^{2030} equation yields an estimated annual carbon-reduction potential in Shanghai in 2030 of:

$$\Delta \mathrm{CO}_2^{2030} = 343,333.40\text{t } CO_2 \ (\text{range} : 311,986.65\text{t } CO_2\text{–}356,550.05\text{t } CO_2) \tag{36}$$

5.5. Cross-City Applicability of the Framework

To further assess the broader applicability of the framework, we examined the full six-month LaDe [27] parcel data from Shanghai, Hangzhou, and Chongqing. As shown in Figure 13, the three cities exhibit similar service-time distributions, tightly overlapping cumulative distributions of point-to-point distance (mean distances: 2.07, 2.84, and 2.99 km), and comparable local parcel clustering at the 1 km, 5 km, and 10 km scales. This cross-city regularity suggests that the parcel-task descriptors used in the present framework are not unique to Shanghai. Accordingly, the framework is likely transferable to other large Chinese cities, although city-specific numerical results still require local recalibration of parcel demand, urban form, airspace constraints, and electricity-related carbon factors.

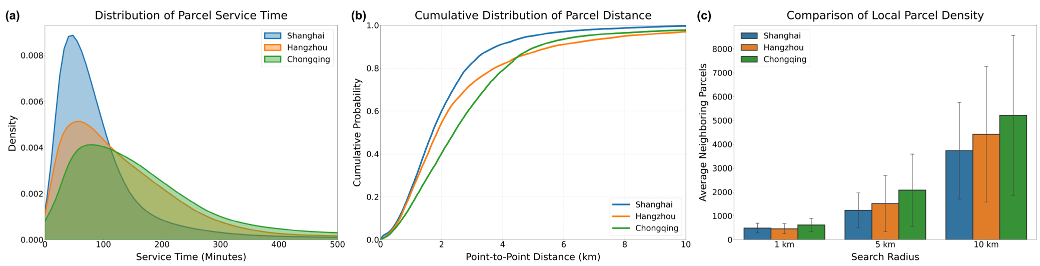

Figure 13. Cross-city comparison of parcel service time, point-to-point distance, and local parcel density for the full six-month LaDe [27] data in Shanghai, Hangzhou, and Chongqing: (**a**) service-time distributions; (**b**) cumulative distributions of point-to-point distance; and (**c**) local parcel density within 1 km, 5 km, and 10 km radii.

5.6. Other Sources of Uncertainty

Although this study establishes a relatively systematic carbon-emission assessment framework and performs calculations and analyses based on real-world data, several sources of uncertainty are inevitable in practical applications: (i) future changes in the grid emission factor EF proportionally rescale the absolute values of E_{UAV} and E_{Courier}, affecting annual totals while typically leaving relative dominance patterns more stable; (ii) the courier speed–energy curve is obtained via scaling a reference trend, and differences in vehicle class and stop-and-go driving cycles can shift E_{Courier}, thus moving the numerical boundaries of critical payloads and the difference matrix; (iii) spatial heterogeneity in obstacles and no-fly zones induces location-specific route geometry, for which we use global averages from reachable trajectories to represent a typical task; (iv) UAV estimates may also vary with the choice of energy-consumption model, as alternative validated quadrotor models report total-energy deviations of less than 8% from the nominal value under Monte-Carlo uncertainty propagation [62]; and (v) real-world last-mile operations may involve failed deliveries or repeated handling, for which published evidence reports failure rates of up to 12% [63], potentially reducing realized carbon benefits if re-delivery is required.

6. Conclusions

Using Shanghai as a representative case, this study develops a unified UAV–courier carbon accounting framework (UCCA) based on over one hundred thousand real-world last-mile express orders and 3D spatial data for a megacity and systematically compares the carbon-emission performance of UAV delivery and conventional courier delivery, yielding the following main findings:

1. By integrating a 3D UAV path-planning algorithm, an empirically calibrated segment-wise UAV energy model, a real-world power-consumption model for large electric courier vehicles, and a medium- to long-term grid emission factor, we propose a last-mile express delivery planning model and carbon-emission assessment pipeline aligned with the Route Design Specification of the Light–Small Unmanned Aircraft System for Urban Logistics. The framework is, in principle, transferable to low-altitude logistics assessments in other Chinese cities, although the numerical outcomes require local recalibration.
2. In the Shanghai case, UAV delivery and conventional courier delivery exhibit only limited differences in parcel-scale delivery geometry, yet they differ substantially in carbon-emission levels. Under light-load and high-speed conditions, UAV delivery shows a lower-carbon advantage in the baseline analysis under the modeled assumptions. The observable sample-comparability analysis further shows that the UAV valid parcel sample (n = 185,673) and the trajectory-linked courier parcel sample (n = 98,210) are broadly similar in service duration, point-to-point distance, and local parcel density, which strengthens the validity of the cross-mode comparison. These findings further suggest that the environmental performance of low-altitude logistics is highly conditional and should be managed through scenario-specific deployment.
3. Based on the carbon-emission difference matrix and the representative 1 kg parcel scenario, full-scale UAV deployment in Shanghai could yield a scenario-based annual carbon reduction of approximately 343,300 t CO_2 by 2030. This magnitude is roughly comparable to the direct carbon emissions of Shanghai's "Metal Products" sector in 2022 [64–69].

In summary, leveraging real operational data and fine-grained spatial constraints, this study quantitatively evaluates carbon emissions from last-mile low-altitude logistics, addressing the lack of systematic analyses of UAV last-mile delivery emissions in the context of Chinese megacities.

The findings suggest that low-altitude logistics could make a meaningful contribution to urban climate mitigation if supported by appropriate operational planning, infrastructure provision, and regulatory design. They further provide scientific evidence to support low-carbon transitions in urban last-mile logistics and the design of low-altitude logistics infrastructure and policy frameworks.

Author Contributions: Conceptualization, Y.L.; Methodology, R.W. and Y.L.; Software, R.W.; Validation, R.W. and Y.L.; Formal Analysis, R.W. and Y.L.; Investigation, R.W.; Resources, R.W.; Data Curation, Y.L.; Visualization, R.W. and Y.L.; Writing—Original Draft Preparation, R.W.; Writing—Review and Editing, Y.L.; Supervision, Y.L.; Funding Acquisition, Y.L. All authors have read and agreed to the published version of the manuscript.

Funding: This research was funded by the Undergraduate Innovation and Practice Training Program of the University of Chinese Academy of Sciences, grant number 20254000040.

Data Availability Statement: Publicly available datasets were analyzed in this study. The LaDe dataset is available from the source cited in Reference [27]. The CMAB building dataset and the OpenSpaceGlobal urban open-space product are available from the sources cited in References [56] and [57], respectively. Some derived data used in this study, including the cleaned station-coordinate dataset and implementation code for the UCCA framework, are available from the corresponding author on reasonable request.

Acknowledgments: The authors thank the developers and maintainers of the publicly available datasets and spatial data sources used in this study. Their efforts in data collection, curation, and dissemination provided important support for this research.

Conflicts of Interest: The authors declare no conflicts of interest.

Abbreviations

The following abbreviations are used in this manuscript:

UAV	Unmanned Aerial Vehicle
UCCA	UAV–Courier Carbon Accounting
API	Application Programming Interface
EF	Emission Factor
ETA	Estimated Time of Arrival
POI	Point of Interest
KD-tree	K-Dimensional Tree
GPS	Global Positioning System
NDCs	Nationally Determined Contributions
CAGR	Compound Annual Growth Rate
CEADs	Carbon Emission Accounts and Datasets
RMB	Renminbi
CMAB	China Multi-Attribute Building dataset
LaDe	Last-mile Delivery dataset
CO_2	Carbon Dioxide
NoFly	No-Fly-zone dataset
DJI Matrice 210 RTK V2	DJI Matrice 210 RTK V2 quadrotor UAV

References

1. Friedlingstein, P.; O'sullivan, M.; Jones, M.W.; Andrew, R.M.; Hauck, J.; Landschützer, P.; Le Quéré, C.; Li, H.; Luijkx, I.T.; Olsen, A.; et al. Global carbon budget 2024. *Earth Syst. Sci. Data Discuss.* **2024**, *17*, 965–1039. [CrossRef]
2. Dhakal, S.; Minx, J.C.; Toth, F.; Abdel-Aziz, A.; Figueroa Meza, M.; Hubacek, K.; Jonckheere, I.G.; Kim, Y.-G.; Nemet, G.F.; Pachauri, S. Emissions trends and drivers (chapter 2). In *Climate Change 2022—Mitigation of Climate Change: Working Group III Contribution to the Sixth Assessment Report of the Intergovernmental Panel on Climate Change*; Cambridge University Press: Cambridge, UK, 2022. [CrossRef]
3. World Economic Forum. *Transforming Urban Logistics: Sustainable and Efficient Last-Mile Delivery in Cities*; World Economic Forum: Geneva, Switzerland, 2024.
4. Liu, Z.; Deng, Z.; He, G.; Wang, H.; Zhang, X.; Lin, J.; Qi, Y.; Liang, X. Challenges and opportunities for carbon neutrality in China. *Nat. Rev. Earth Environ.* **2022**, *3*, 141–155. [CrossRef]
5. Wang, H.-L.; Weng, Y.-Y.; Pan, X.-Z. Comparison and analysis of mitigation ambitions of Parties' updated Nationally Determined Contributions. *Adv. Clim. Change Res.* **2023**, *14*, 4–12. [CrossRef]
6. Ao, Z.; Fei, R.; Jiang, H.; Cui, L.; Zhu, Y. How can China achieve its goal of peaking carbon emissions at minimal cost? A research perspective from shadow price and optimal allocation of carbon emissions. *J. Environ. Manag.* **2023**, *325*, 116458. [CrossRef] [PubMed]
7. Chen, X.H.; Tee, K.; Elnahass, M.; Ahmed, R. Assessing the environmental impacts of renewable energy sources: A case study on air pollution and carbon emissions in China. *J. Environ. Manag.* **2023**, *345*, 118525. [CrossRef] [PubMed]
8. Hepburn, C.; Qi, Y.; Stern, N.; Ward, B.; Xie, C.; Zenghelis, D. Towards carbon neutrality and China's 14th Five-Year Plan: Clean energy transition, sustainable urban development, and investment priorities. *Environ. Sci. Ecotechnol.* **2021**, *8*, 100130. [CrossRef]
9. Zhong, Y.; Cui, S.; Bai, X.; Shang, W.; Huang, W.; Liu, L.; Wang, S.; Zhu, R.; Zhai, Y.; Zhang, Y. Carbon emissions from urban takeaway delivery in China. *npj Urban Sustain.* **2024**, *4*, 39. [CrossRef]
10. Saenz, J.; Figliozzi, M.; Faulin, J. Assessment of the Carbon Footprint Reductions of Tricycle Logistics Services. *Transp. Res. Rec.* **2016**, *2570*, 48–56. [CrossRef]
11. Saenz-Esteruelas, J.; Figliozzi, M.; Serrano, A.; Faulin, J. Electrifying Last-Mile Deliveries: A Carbon Footprint Comparison between Internal Combustion Engine and Electric Vehicles. In *Proceedings of the Smart Cities*; Springer Nature: Cham, Switzerland, 2016; pp. 76–84.
12. Dong, Y.; Guo, X.; Wang, M.; Xu, J. Modeling carbon intensity of electric vehicles in the well-to-wheels phase under different traffic flow conditions. *iScience* **2024**, *27*, 111070. [CrossRef]
13. Stolaroff, J.K.; Samaras, C.; O'Neill, E.R.; Lubers, A.; Mitchell, A.S.; Ceperley, D. Energy use and life cycle greenhouse gas emissions of drones for commercial package delivery. *Nat. Commun.* **2018**, *9*, 409. [CrossRef]
14. China Academy of Information and Communications Technology. *Low-Altitude Economy: Policy and Industrial Ecosystem Development in China*; China Academy of Information and Communications Technology (CAICT): Beijing, China, 2024.
15. Doole, M.; Ellerbroek, J.; Hoekstra, J. Estimation of traffic density from drone-based delivery in very low level urban airspace. *J. Air Transp. Manag.* **2020**, *88*, 101862. [CrossRef]
16. Eichleay, M.; Evens, E.; Stankevitz, K.; Parker, C. Using the Unmanned Aerial Vehicle Delivery Decision Tool to Consider Transporting Medical Supplies via Drone. *Glob. Health Sci. Pract.* **2019**, *7*, 500. [CrossRef]
17. Li, Z.; Li, S.; Lu, J.; Wang, S. Air Route Network Planning Method of Urban Low-Altitude Logistics UAV with Double-Layer Structure. *Drones* **2025**, *9*, 193. [CrossRef]
18. Murray, C.C.; Chu, A.G. The flying sidekick traveling salesman problem: Optimization of drone-assisted parcel delivery. *Transp. Res. Part C Emerg. Technol.* **2015**, *54*, 86–109. [CrossRef]
19. Sadeghi Esfahlani, S.; Simanjuntak, S.; Sanaei, A.; Fraess-Ehrfeld, A. Advanced Drone Routing and Scheduling for Emergency Medical Supply Chains in Essex. *Drones* **2025**, *9*, 664. [CrossRef]
20. Securities Times. With 740,000 Commercial Orders, Meituan Accelerates Its UAV Rollout as JD.com, FlashEx and Other Giants Double Down on the "Low-Altitude Battlefield" of Instant Retail. *Securities Times*, 23 December 2025.
21. Touch Shanghai. Delivery Descends from the Sky! Meituan's First Regular Commercial Drone Route Is Officially Launched in Shanghai! *Touch Shanghai*, 6 May 2023.
22. Brown, J.R.; Bushuev, M.A. Last mile delivery with drones: A carbon emissions comparison. *Int. J. Sustain. Transp.* **2024**, *18*, 791–802. [CrossRef]
23. Figliozzi, M.A. Lifecycle modeling and assessment of unmanned aerial vehicles (Drones) CO2e emissions. *Transp. Res. Part D Transp. Environ.* **2017**, *57*, 251–261. [CrossRef]
24. Goodchild, A.; Toy, J. Delivery by drone: An evaluation of unmanned aerial vehicle technology in reducing CO_2 emissions in the delivery service industry. *Transp. Res. Part D Transp. Environ.* **2018**, *61*, 58–67. [CrossRef]
25. Kirschstein, T. Comparison of energy demands of drone-based and ground-based parcel delivery services. *Transp. Res. Part D Transp. Environ.* **2020**, *78*, 102209. [CrossRef]

26. Shanghai Municipal Commission of Economy and Informatization. *Shanghai's 14th Five-Year Plan for Industrial Green Development*; Shanghai Municipal Commission of Economy and Informatization: Shanghai, China, 2022.
27. Wu, L.; Wen, H.; Hu, H.; Mao, X.; Xia, Y.; Shan, E.; Zheng, J.; Lou, J.; Liang, Y.; Yang, L.; et al. LaDe: The First Comprehensive Last-mile Express Dataset from Industry. In *Proceedings of the 30th ACM SIGKDD Conference on Knowledge Discovery and Data Mining, Barcelona, Spain, 25–29 August 2024*; Association for Computing Machinery: New York, NY, USA, 2024; pp. 5991–6002.
28. Sartori, D.; Zou, D.; Yu, W. An efficient approach to near-optimal 3D trajectory design in cluttered environments for multirotor UAVs. In *Proceedings of the 2019 IEEE 15th International Conference on Automation Science and Engineering (CASE), Vancouver, BC, Canada, 22–26 August 2019*; IEEE Press: Piscataway, NJ, USA, 2019; pp. 1016–1022.
29. Almasan, P.; Suárez-Varela, J.; Rusek, K.; Barlet-Ros, P.; Cabellos-Aparicio, A. Deep reinforcement learning meets graph neural networks: Exploring a routing optimization use case. *Comput. Commun.* **2022**, *196*, 184–194. [CrossRef]
30. Li, X.; Luo, W.; Yuan, M.; Wang, J.; Lu, J.; Wang, J.; Lu, J.; Zeng, J. Learning to Optimize Industry-Scale Dynamic Pickup and Delivery Problems. In *Proceedings of the 2021 IEEE 37th International Conference on Data Engineering (ICDE), Chania, Greece, 19–22 April 2021*; IEEE Press: Piscataway, NJ, USA, 2021; pp. 2511–2522.
31. Zeng, Y.; Tong, Y.; Chen, L. Last-mile delivery made practical: An efficient route planning framework with theoretical guarantees. *Proc. VLDB Endow.* **2019**, *13*, 320–333. [CrossRef]
32. Gao, C.; Zhang, F.; Wu, G.; Hu, Q.; Ru, Q.; Hao, J.; He, R.; Sun, Z. A Deep Learning Method for Route and Time Prediction in Food Delivery Service. In *Proceedings of the 27th ACM SIGKDD Conference on Knowledge Discovery & Data Mining, Virtual Event, Singapore, 14–18 August 2021*; Association for Computing Machinery: New York, NY, USA, 2021; pp. 2879–2889.
33. Araujo, A.C.d.; Etemad, A. End-to-End Prediction of Parcel Delivery Time With Deep Learning for Smart-City Applications. *IEEE Internet Things J.* **2021**, *8*, 17043–17056. [CrossRef]
34. Wu, F.; Wu, L. DeepETA: A Spatial-Temporal Sequential Neural Network Model for Estimating Time of Arrival in Package Delivery System. *Proc. AAAI Conf. Artif. Intell.* **2019**, *33*, 774–781. [CrossRef]
35. Li, K. Study on the Layout of Express Outlets in Beijing Based on Machine Learning. Master's Thesis, Beijing Jiaotong University, Beijing, China, 2019. (In Chinese)
36. Dorling, K.; Heinrichs, J.; Messier, G.G.; Magierowski, S. Vehicle Routing Problems for Drone Delivery. *IEEE Trans. Syst. Man Cybern. Syst.* **2017**, *47*, 70–85. [CrossRef]
37. Zhang, J.; Campbell, J.F.; Sweeney, D.C., II; Hupman, A.C. Energy consumption models for delivery drones: A comparison and assessment. *Transp. Res. Part D Transp. Environ.* **2021**, *90*, 102668. [CrossRef]
38. Franco, C.D.; Buttazzo, G. Energy-Aware Coverage Path Planning of UAVs. In *Proceedings of the 2015 IEEE International Conference on Autonomous Robot Systems and Competitions, Vila Real, Portugal, 8–10 April 2015*; IEEE Press: Piscataway, NJ, USA, 2015; pp. 111–117.
39. Abeywickrama, H.V.; Jayawickrama, B.A.; He, Y.; Dutkiewicz, E. Comprehensive Energy Consumption Model for Unmanned Aerial Vehicles, Based on Empirical Studies of Battery Performance. *IEEE Access* **2018**, *6*, 58383–58394. [CrossRef]
40. Gong, H.; Huang, B.; Jia, B.; Dai, H. Modeling Power Consumptions for Multirotor UAVs. *IEEE Trans. Aerosp. Electron. Syst.* **2023**, *59*, 7409–7422. [CrossRef]
41. Mellios, G.; Hausberger, S.; Keller, M.; Samaras, C.; Ntziachristos, L. *Parameterisation of Fuel Consumption and CO_2 Emissions of Passenger Cars and Light Commercial Vehicles for Modelling Purposes*; Publications Office of the European Union: Luxembourg City, Luxembourg, 2011. [CrossRef]
42. Weiss, M.; Cloos, K.C.; Helmers, E. Energy efficiency trade-offs in small to large electric vehicles. *Environ. Sci. Eur.* **2020**, *32*, 46. [CrossRef]
43. Grée, F.; Laznikova, V.; Kim, B.; Garcia, G.; Kigezi, T.; Gao, B. Cloud-Based Big Data Platform for Vehicle-to-Grid (V2G). *World Electr. Veh. J.* **2020**, *11*, 30. [CrossRef]
44. Ohde, B.; Ślaski, G.; Maciejewski, M. Statistical analysis of real-world urban driving cycles for modelling energy consumption of electric vehicles. *J. Mech. Transp. Eng.* **2016**, *68*, 25–39. [CrossRef]
45. Kusalaphirom, T.; Satiennam, T.; Satiennam, W. Factors Influencing the Real-World Electricity Consumption of Electric Motorcycles. *Energies* **2023**, *16*, 6369. [CrossRef]
46. Liang, Y.; Juntong, Q.; Xiao, J.; Xia, Y. A literature review of UAV 3D path planning. In *Proceedings of the 11th World Congress on Intelligent Control and Automation, Shenyang, China, 29 June–4 July 2014*; IEEE Press: Piscataway, NJ, USA, 2014; pp. 2376–2381.
47. Hart, P.E.; Nilsson, N.J.; Raphael, B. A Formal Basis for the Heuristic Determination of Minimum Cost Paths. *IEEE Trans. Syst. Sci. Cybern.* **1968**, *4*, 100–107. [CrossRef]
48. Koenig, S.; Likhachev, M. Incremental A*. In *Proceedings of the 15th International Conference on Neural Information Processing Systems: Natural and Synthetic, Vancouver, BC, Canada, 3–8 December 2001*; MIT Press: Cambridge, MA, USA, 2001; pp. 1539–1546.
49. Stentz, A. The focussed D* algorithm for real-time replanning. In *Proceedings of the 14th International Joint Conference on Artificial Intelligence—Volume 2, Montreal, QC, Canada, 20–25 August 1995*; Morgan Kaufmann Publishers: San Francisco, CA, USA, 1995; pp. 1652–1659.

50. Daniel, K.; Nash, A.; Koenig, S.; Felner, A. Theta*: Any-angle path planning on grids. *J. Artif. Intell. Res.* **2010**, *39*, 533–579. [CrossRef]
51. Nash, A.; Koenig, S.; Tovey, C. Lazy Theta*: Any-Angle Path Planning and Path Length Analysis in 3D. *Proc. AAAI Conf. Artif. Intell.* **2010**, *24*, 147–154. [CrossRef]
52. Ministry of Ecology and Environment of the People's Republic of China; National Bureau of Statistics of China; National Energy Administration. *Announcement on Releasing the 2024 Electricity Carbon Footprint Factor Data*; Ministry of Ecology and Environment of the People's Republic of China: Beijing, China, 2025. (In Chinese)
53. Cai, B.; Zhao, L.; Zhang, Z. Research on Carbon Dioxide Emission Factors of China's Regional Power Grid (2020–2035). Available online: https://www.caep.org.cn/sy/tdftzhyjzx/zxdt/202310/W020231027692141725225.pdf (accessed on 20 December 2025). (In Chinese)
54. Shanghai Municipal Statistics Bureau. *Statistical Bulletin on National Economic and Social Development of Shanghai (2024)*; Shanghai Municipal Statistics Bureau: Shanghai, China, 2025. (In Chinese)
55. Shanghai Postal Administration. *Shanghai Postal Industry Development Statistical Bulletin (2024)*; Shanghai Postal Administration: Shanghai, China, 2025. (In Chinese)
56. Zhang, Y.; Zhao, H.; Long, Y. CMAB: A Multi-Attribute Building Dataset of China. *Sci. Data* **2025**, *12*, 430. [CrossRef]
57. Fan, R.; Wang, L.; Xu, Z.; Niu, H.; Chen, J.; Zhou, Z.; Li, W.; Wang, H.; Sun, Y.; Feng, R. The first urban open space product of global 169 megacities using remote sensing and geospatial data. *Sci. Data* **2025**, *12*, 586. [CrossRef]
58. *MH/T 4054—2022*; Route Design Specification of the Light-Small Unmanned Aircraft System for Urban Logistics. Civil Aviation Administration of China: Beijing, China, 2022. (In Chinese)
59. DJI. Matrice 200 Series V2 Support [Product Information]. Available online: https://www.dji.com/cn/support/product/matrice-200-series-v2 (accessed on 28 November 2025).
60. Bentley, J.L. Multidimensional binary search trees used for associative searching. *Commun. ACM* **1975**, *18*, 509–517. [CrossRef]
61. Kang, P.; Song, G.; Xu, M.; Miller, T.R.; Wang, H.; Zhang, H.; Liu, G.; Zhou, Y.; Ren, J.; Zhong, R.; et al. Low-carbon pathways for the booming express delivery sector in China. *Nat. Commun.* **2021**, *12*, 450. [CrossRef]
62. Głębocki, R.; Żugaj, M.; Jacewicz, M. Validation of the energy consumption model for a quadrotor using Monte-Carlo simulation. *Arch. Mech. Eng.* **2023**, *70*, 151–178. [CrossRef]
63. Xia, W. Research on the application and multi-dimensional economic impact of unmanned delivery vehicles in e-commerce terminal delivery. *E-Commer. Lett.* **2025**, *14*, 1428–1435. (In Chinese) [CrossRef]
64. Xu, J.; Guan, Y.; Oldfield, J.; Guan, D.; Shan, Y. China carbon emission accounts 2020–2021. *Appl. Energy* **2024**, *360*, 122837. [CrossRef]
65. Carbon Emission Accounts and Datasets (CEADs). Available online: https://www.ceads.net.cn (accessed on 12 November 2025).
66. Guan, Y.; Shan, Y.; Huang, Q.; Chen, H.; Wang, D.; Hubacek, K. Assessment to China's Recent Emission Pattern Shifts. *Earth's Future* **2021**, *9*, e2021EF002241. [CrossRef]
67. Shan, Y.; Huang, Q.; Guan, D.; Hubacek, K. China CO_2 emission accounts 2016–2017. *Sci. Data* **2020**, *7*, 54. [CrossRef] [PubMed]
68. Shan, Y.; Guan, D.; Zheng, H.; Ou, J.; Li, Y.; Meng, J.; Mi, Z.; Liu, Z.; Zhang, Q. China CO_2 emission accounts 1997–2015. *Sci. Data* **2018**, *5*, 170201. [CrossRef]
69. Shan, Y.; Liu, J.; Liu, Z.; Xu, X.; Shao, S.; Wang, P.; Guan, D. New provincial CO_2 emission inventories in China based on apparent energy consumption data and updated emission factors. *Appl. Energy* **2016**, *184*, 742–750. [CrossRef]